Congenital disorder of glycosylation caused by starting site-specific variant in syntaxin-5

Peter T.A. Linders[1], Eveline C.F. Gerretsen[1], Angel Ashikov[2,3], Mari-Anne Vals[4,5], Rinse de Boer[6], Natalia H. Revelo[1], Richard Arts[1], Melissa Baerenfaenger[2], Fokje Zijlstra[3], Karin Huijben[3], Kimiyo Raymond[7], Kai Muru[5,8], Olga Fjodorova[8], Sander Pajusalu[5,8], Katrin Õunap[5,8], Martin ter Beest[1], Dirk Lefeber[2,3,*] and Geert van den Bogaart[1,9,*]

[1] Department of Tumor Immunology, Radboud Institute for Molecular Life Sciences, Radboud University Medical Center, 6525 GA Nijmegen, The Netherlands

[2] Department of Neurology, Donders Institute for Brain, Cognition and Behavior, Radboud University Medical Center, 6525 GA, Nijmegen, The Netherlands

[3] Translational Metabolic Laboratory, Department of Laboratory Medicine, Radboud University Medical Center, 6525 GA, Nijmegen, The Netherlands

[4] Children's Clinic, Tartu University Hospital, Estonia

[5] Department of Clinical Genetics, Institute of Clinical Medicine, University of Tartu, Estonia

[6] Molecular Cell Biology, Groningen Biomolecular Sciences and Biotechnology Institute, University of Groningen, Groningen, The Netherlands

[7] Department of Laboratory Medicine and Pathology, Mayo College of Medicine, Rochester, Minnesota, USA.

[8] Department of Clinical Genetics, United Laboratories, Tartu University Hospital, Tartu, Estonia

[9] Department of Molecular Immunology, Groningen Biomolecular Sciences and Biotechnology Institute, University of Groningen, 9747AG, Groningen, Netherlands

[*] Correspondence: dirk.lefeber@radboudumc.nl; Tel.: +31-24-36-14567; g.van.den.bogaart@rug.nl; Tel.: +31-50-36-35230

Abstract

The SNARE (soluble N-ethylmaleimide-sensitive factor attachment protein receptor) protein syntaxin-5 (Stx5) is essential for Golgi transport. In humans, the *STX5* mRNA encodes two protein isoforms, Stx5 Long (Stx5L) from the first starting methionine and Stx5 Short (Stx5S) from an alternative starting methionine at position 55. In this study, we identified a novel human disorder caused by a single missense substitution in the second starting

methionine (p.M55V), resulting in complete loss of the short isoform. Patients suffer from an early fatal multisystem disease, including severe liver disease, skeletal abnormalities and abnormal glycosylation. Primary human dermal fibroblasts isolated from these patients showed defective glycosylation, altered Golgi morphology as measured by electron microscopy and mislocalization of glycosyltransferases. Measurements of anterograde trafficking, based on biotin-synchronizable forms of Stx5 (the RUSH system), and of cognate binding SNAREs, based on Förster resonance energy transfer (FRET), revealed that the short isoform of Stx5 is essential for intra-Golgi transport. This is the first time a mutation in an alternative starting codon is linked to human disease, demonstrating that the site of translation initiation is an important new layer of regulating protein trafficking.

Keywords

Syntaxin-5, ER-Golgi trafficking, glycosylation, secretory pathway, congenital disorders of glycosylation

42 **Introduction**

43 In eukaryotes, proteins destined for the secretory pathway are synthesized at the endoplasmic reticulum (ER)
44 and then transported to the Golgi apparatus, where they are sorted for their ultimate destinations at the *trans*-
45 Golgi network. Central to this process is intracellular membrane fusion, which is mediated by members of the
46 SNARE (soluble *N*-ethylmaleimide-sensitive factor attachment protein receptor) protein family. Cognate SNARE
47 proteins that are present in both the carrier vesicle and target membranes, called v- and t-SNAREs respectively,
48 engage and form a tight alpha-helical coiled-coil bundle that overcomes the energy barrier of membrane fusion.
49 Membrane fusion requires a single R-SNARE, characterized by an arginine residue located central in the SNARE
50 bundle, and three Q-SNAREs, with glutamine residues instead. Generally in mammalian cells, the R-SNAREs act
51 as vesicle (v-) SNAREs and the Q-SNAREs together form the t-SNARE complex on the target membrane[1]. In
52 contrast, the Qc-SNAREs Bet1 and Bet1L (GS15) function as the v-SNAREs at the ER/Golgi interface[2–5], while, for
53 anterograde ER to Golgi trafficking, the recipient t-SNARE complex is formed by the Qa-SNARE syntaxin-5 (Stx5)[6–
54 9], together with the Qb-SNAREs GosR1 (also known as GS27 or membrin) or GosR2 (GS28), and R-SNAREs Ykt6
55 or Sec22b (Ers24)[10–12]. This different allocation of the Qc-SNAREs Bet1 and Bet1L as v-SNARE instead of t-SNARE
56 possibly prevents the formation of non-functional SNARE complexes during ER to Golgi transit. In addition, Stx5
57 functions in retrograde intra-Golgi transport by forming a recipient t-SNARE complex with GosR1, and Ykt6[5,13]
58 and in retrograde trafficking from endosomes to the *trans*-Golgi network (TGN)[14,15], making it a unique SNARE
59 protein involved in both anterograde and retrograde Golgi transport.

60 *STX5* is highly conserved and is an essential gene in animals and fungi[16,17]. In animals, Stx5 exists as a long and a
61 short isoform translated from the same mRNA: 39.6 kDa sized Stx5 Long (Stx5L) and 34.1 kDa sized Stx5 Short
62 (Stx5S)[13,18]. This is in contrast to lower organisms such as *Saccharomyces cerevisiae*, which only express a single
63 isoform of Stx5 (Sed5p). Although Sed5p was originally believed to resemble mammalian Stx5S[13], it is now clear
64 that it likely more resembles Stx5L, since an N-terminal COPI-binding tribasic motif has been identified in
65 Sed5p[19]. The emergence of a second Stx5 isoform can be traced back to the pacific purple sea urchin,
66 *Strongylocentrotus purpuratus,* and is also present in the model organism *Danio rerio*, but not in *Drosophila*
67 *melanogaster* nor *Caenorhabditis elegans*. Compared to Stx5S, Stx5L contains 54 extra N-terminal residues
68 bearing an Arginine – Lysine – Arginine (RKR) ER retrieval motif, and as a result, Stx5L locates more to the ER
69 whereas Stx5S locates more to the Golgi network[13,18,20–22]. The evolutionary necessity of the two Stx5 isoforms
70 remains unclear but it has been suggested that Stx5L is important to maintain ER structure by binding

71 microtubules, possibly via CLIMP-63[21,23]. In addition, immunoprecipitations showed that GosR1 and Bet1L
72 preferentially interact with Stx5S over Stx5L[24,25], suggesting that Stx5S might act in more fusogenic complexes
73 later at the ER-Golgi interface whereas Stx5L might be more involved in earlier fusion steps.
74 In the present study, we identified a genetic variant in the second translation codon methionine-55, fully
75 abrogating the production of Stx5S and providing a unique opportunity to study the physiological relevance of
76 the existence of two isoforms in humans. Patients homozygous for this mutation have a very severe clinical
77 phenotype associated with infantile mortality and defective protein glycosylation. We demonstrate that
78 although Stx5L can largely compensate for the lack of Stx5S, the loss of Stx5S leads to defects in intra-Golgi
79 trafficking with mislocalization of glycosyltransferases, which results in pronounced defects in glycosylation.
80 Moreover, by synchronizing the intracellular trafficking of Stx5 isoforms, we reveal differential trafficking routes
81 for either isoform and identify Stx5S as the dominant Qa-SNARE for intra-Golgi transport. This is the first time
82 that a mutation in an alternate starting site of ribosomal translation is related to human disease. This finding
83 reveals that protein function can be regulated at the level of translation initiation and has profound effects on
84 intracellular membrane trafficking and Golgi function.
85
86 **Results**
87 ***Clinical data***
88 The family history (Supplementary Fig. 1) revealed multiple deceased individuals (IV:3, IV:9, IV:10) shortly after
89 birth, spontaneous abortions (IV:5, IV:6, IV:7), and elective abortions in the 20th-21st week of pregnancy due to
90 abnormal fetal ultrasound (US) (IV:4, IV:8). Fetal US of individuals IV:8, IV:9, and IV:10 (Fig. 1a-c, respectively)
91 showed shortening of the long bones with suspicion of chondrodysplasia. Patients IV:9 and IV:10 showed highly
92 dysmorphic facial features (high forehead, frontal bossing, prominent glabella, short and upturned nose, long
93 philtrum, micrognathia and dysplastic ears), skeletal dysplasia (short extremities and narrow thorax), profound
94 hypotonia, hepatomegaly, and many abnormal laboratory parameters including elevated cholesterol (Fig. 1b, c,
95 Supplementary Table 1). After birth, the main clinical problem for both patients IV:9 and IV:10 was progressive
96 liver failure with cholestasis and hyperinsulinemic hypoglycemia (Supplementary Table 1). Liver failure was the
97 main cause of death at the age of between 0 and 3 month, and between 6 and 9 months, in patients IV:9 and
98 IV:10, respectively. Autopsy of fetus IV:8 revealed bilateral hydronephrosis and sacral lordosis. Autopsy of
99 patient IV:9 showed hepatomegaly with stage 3 to 4 liver fibrosis, agenesis of left kidney, hyperemia of internal

organs, ventricular septal defect and suggestive pathohistological features of chondrodysplasia. Autopsy of patient IV:10 showed biliary cirrhosis and nodular regenerative hyperplasia, pancreatic hypertrophia/hyperplasia, and narrow thorax with normal lung development.

Abnormal protein glycosylation suggests a defect in Golgi trafficking

Known genetic causes for skeletal dysplasias were excluded (IV:8), no submicroscopic chromosomal abnormalities were found, while most metabolic investigations were normal except for the Congenital Disorders of Glycosylation (CDG) (IV:9 and IV:10). CDG screening revealed a strong hyposialylation of protein N-glycosylation and mucin-type O-glycosylation, as analyzed by isofocusing of respectively plasma transferrin (Fig. 1d, Supplementary Table 2) and apolipoprotein CIII (ApoCIII-IEF, Fig. 1e, Supplementary Table 2). ApoCIII-IEF showed a strong increase of non-sialylated apoCIII (ApoCIII-0) band intensities compared to the intensities of the fully glycosylated form, even stronger than observed for genetic defects in the Conserved Oligomeric Golgi (COG) complex, a known group of disorders with disturbed Golgi homeostasis and abnormal glycosylation[26].

To gain more insight into the abnormal N-glycan structures, mass spectrometry was performed of intact transferrin (Fig. 1f, g, Supplementary Fig. 2) and of total plasma protein derived N-glycans (Fig. 1f, h, Supplementary Fig. 3). Analysis of intact transferrin of individuals IV:9 and IV:10 revealed multiple abnormal glycan structures, divided into two categories: high mannose structures and truncated glycans. Compared to the peak height of completely glycosylated transferrin, a dominant accumulation was found of high-mannose glycans (Supplementary Table 3, Man5, mass/peak number) suggesting a problem with MGAT1, the enzyme that adds the next *N*-acetylglucosamine during N-glycosylation. Furthermore, a series of transferrin isoforms was observed with reduced incorporation of galactose and sialic acid residues. Similar glycosylation patterns were observed in COG5-CDG[27–30]. Analysis of N-glycans released from total plasma proteins recapitulated the two categories of abnormal glycans with the accumulation of high mannose glycans, as well as reduced incorporation of galactose and sialic acid residues (Supplementary Table 4). Together, these data indicate that the activities of multiple glycosyltransferases in the Golgi apparatus are affected, covering both N- and O-glycosylation, thereby suggesting a general disturbance in Golgi trafficking.

Molecular investigations result in the identification of variants in STX5

128 Chromosomal microarray analysis (CMA) using HumanCytoSNP-12 microarrays revealed multiple long
129 contiguous stretches of homozygosity (LCSH, >5 Mb) distributed across the entire genome, with several regions
130 of homozygosity on chromosome 11 in all three affected sibs (IV:8, IV:9 and IV:10, Supplementary Table 5).
131 Exome sequencing was performed in proband IV:9 to find the genetic variant that could be associated with the
132 disease. Only two homozygous rare protein-altering variants without homozygous individuals in the gnomAD v3
133 database were identified in shared homozygous stretches on chromosome 11. First, a missense variant in the
134 *VPS37C* gene was discovered (NM_017966.4:c.760G>T p.(Gly254Cys) rs201088253). However, as this variant
135 reaches an allele frequency of 0.9% in Estonia, it is unlikely to cause a rare genetic disorder. The second variant
136 was identified in the *STX5* gene (NM_003164.4:c.163A>G p.(Met55Val), Fig 2a). This is a missense mutation
137 affecting the alternative starting codon for the production of the short Stx5 isoform. The variant is absent from
138 the gnomAD v3 database and was thus classified as a potentially disease-causing variant. The variant was
139 confirmed by Sanger sequencing as homozygous in all affected individuals (IV:8, IV:9, and IV:10) and as
140 heterozygous in the mother (III:2). Paternal DNA was not available for testing.
141 To confirm the effect of the genetic variant on both Stx5 proteoforms, immunoblotting was performed in
142 primary dermal fibroblasts of patients IV:9 and IV:10. While Stx5L was present, a total absence of Stx5S was
143 found in both patient fibroblasts (Fig. 2b, c). We next tested the expression of known interaction partners of
144 Stx5. The levels of Qc-SNARE Bet1L, which forms a complex with Stx5 upon retrograde intra-Golgi trafficking[5,13–
145 15], were also reduced. In contrast (Fig. 2b, c), the expression of Qc-SNARE Bet1, which forms a complex with
146 Stx5 upon anterograde ER-Golgi trafficking[10,12,13,31] was not reduced (Fig. 2b, c). Likewise, the expression of Qb-
147 SNAREs GosR1 and GosR2, which can complex with Stx5 for anterograde ER-Golgi trafficking and retrograde
148 intra-Golgi trafficking[5,9,10,12,13,24] were unaltered in patient dermal fibroblast lysates. We hypothesized that a
149 compensatory mechanism might exist by upregulating the expression of the *trans*-Golgi Qa-SNARE Stx16[32],
150 usually involved in endosome-to-TGN trafficking[33], but we did not detect a change of Stx16 expression in patient
151 fibroblast lysates (Fig. 2b, c). As a first step to confirm that fibroblasts offer a useful model to recapitulate the
152 cell biological abnormalities due to loss of the Stx5S isoform, we studied glycosylation by fluorescently-labeled
153 lectins.
154
155 ***Glycosylation defects in Stx5M55V patient fibroblasts***

156 Patient fibroblasts could be cultured normally and we did not observe apparent differences in growth rate or
157 viability between healthy control and patient-derived cell lines. Cell surface staining with the lectin SNA-I from
158 *Sambucus nigra*, which binds terminal sialic acid in an α-2,6 linkage of fully-formed N-glycan moieties and, to a
159 lesser extent, sialic acid in an α-2,3 linkage, showed that glycosylation was also impaired at the cellular level in
160 patient fibroblasts. Compared to fibroblasts of healthy donors, we observed a more than two-fold reduced SNA-
161 I labeling intensity in Stx5M55V patient fibroblasts (Fig. 2d,e). Moreover, most signal came from punctuated
162 structures in the Stx5M55V patient fibroblasts, instead of the more uniform cell membrane labeling observed in
163 the healthy donor fibroblasts. To confirm this glycosylation defect, we performed cell surface staining with the
164 lectin PNA (Peanut agglutinin) from *Arachis hypogaea*, which binds terminal galactose residues present on mucin
165 O-glycan moieties of incompletely glycosylated proteins. Opposite to our findings with SNA-I, we observed an
166 increased labeling intensity in Stx5M55V patient fibroblasts relative to healthy control by about six-fold (Fig.
167 2f,g). These findings show that patient-derived fibroblasts, which express Stx5L but lack Stx5S, have a
168 glycosylation defect.
169 Next, we evaluated the expression levels of Stx5S and Stx5L in lysates of peripheral blood mononuclear cells
170 (PBMCs) obtained from four different healthy donors (Supplementary Fig. 4). While total Stx5 expression levels
171 varied strongly (more than two-fold), the ratio of Stx5S and Stx5L was approximately equimolar for all
172 individuals, demonstrating that the expression ratio is similar in PBMCs of different healthy subjects.
173 To determine the role of Stx5S in Golgi transport, we generated a Stx5L-lacking fibroblast cell line from one of
174 the prior used control lines, using CRISPR/Cas9 (Fib Stx5ΔL, Supplementary Fig. 5a). We then performed the
175 same cell surface staining as described above. While we observed a similar decrease in SNA-I labeling intensity
176 in Stx5ΔL fibroblasts as in Stx5M55V patient fibroblasts, the staining pattern was more similar to healthy control
177 and showed a uniform plasma membrane-localized SNA-I labeling (Supplementary Fig. 5b-c). In addition,
178 opposite to Stx5M55V fibroblasts, the low PNA labeling intensity was reduced further in Fib Stx5ΔL
179 (Supplementary Fig. 5d-e). To investigate this difference further, we generated two clonal HeLa cell lines lacking
180 Stx5L using the same method (Stx5ΔL: B1A7 and C1F4, Supplementary Fig. 5f), and we observed a decrease in
181 the already low SNA-I labeling intensity as measured by FACS compared to the parental HeLa cells, while PNA
182 labeling resulted in opposite changes between the two Stx5ΔL lines (Supplementary Fig. 5g-k). The difference in
183 PNA labeling between the HeLa Stx5ΔL cell lines therefore likely is attributable by clonal variation and/or off-

184 target effects of CRISPR/Cas9. These results demonstrate that while the loss of Stx5S or Stx5L both result in N-
185 glycosylation defects, the defect is stronger upon the loss of Stx5S, as this results in lower levels and a
186 punctuated distribution of sialic acid moieties. Moreover, the mucin-type O-glycosylation defect seems specific
187 to the loss of Stx5S. As these results reiterate the glycosylation defect observed on serum transferrin, total
188 plasma N-glycans and apoCIII mucin O-glycans, patient fibroblasts are a suitable model to investigate the cell
189 biological consequences of the complete disruption of the Stx5S isoform.
190
191 ***Stx5M55V mutation results in mislocalization of glycosyltransferases***
192 Given that Stx5 mediates ER-Golgi trafficking[5,7,9–13,15,24,31], we next investigated whether the glycosylation defect
193 in Stx5M55V patient fibroblasts was caused by the mislocalization of glycosyltransferases. We performed
194 immunofluorescence labeling of mannosyl (α-1,3)-glycoprotein β-1,2-*N*-acetylglucosaminyltransferase (MGAT1,
195 also known as GnTI), which catalyzes the addition of GlcNAc to the immature man-5 N-glycan. Compared to
196 healthy donor fibroblasts, MGAT1 colocalizes only slightly less with the *cis*-Golgi marker GM130 in patient
197 fibroblasts (Fig. 3a, b), but colocalized substantially less with the *trans*-Golgi network marker TGN46 (Fig. 3c, d).
198 In addition, alpha-mannosidase 2 (MAN2A1), which catalyzes the final hydrolytic step in the N-glycan maturation
199 pathway after MGAT1 conversion, colocalized substantially less with both GM130 (Supplementary Fig. 6a, b)
200 and TGN46 in patient fibroblasts (Supplementary Fig. 6c, d). Similarly to MGAT1, beta-galactoside alpha-2,6-
201 sialyltransferase 1 (ST6GAL1), which catalyzes the transfer of sialic acid to galactose residues of N-glycans in an
202 α-2,6 linkage, colocalized less with both GM130 (Supplementary Fig. 6e, f) and TGN46 in patient fibroblasts
203 (Supplementary Fig. 6g, h). Finally, *N*-acetylgalactosaminyltransferase 2 (GALNT2), which catalyzes the initial
204 reaction in mucin O-linked glycan synthesis, localized more to the *cis*-Golgi (marker Zinc finger protein-like 1
205 (ZFPL1)[35]) (Fig. 3e, f) and less to the *trans*-Golgi in patient fibroblasts (Fig. 3g, h).
206 To exclude the possibility that our conclusions were affected by potential mislocalization of TGN46 in the patient
207 cells, we repeated these experiments but now co-stained for another *trans*-Golgi marker, the *trans*-Golgi coiled-
208 coil protein p230[36] (Supplementary Fig. 7). Indeed, we observed similar Pearson correlation coefficients for p230
209 as for TGN46 with MGAT1, GALNT2, MAN2A1, and ST6GAL1 (Supplementary Fig. 7). Moreover, to confirm that
210 the observed changes in colocalization were not due to lower expression of glycosyltransferases, we performed
211 immunoblotting for several glycosyltransferases and could not detect consistent differences between control
212 and Stx5M55V fibroblasts, although we noticed substantial variation in protein expression levels of some of the

213 glycosyltransferases between the samples (Supplementary Fig. 8), reflecting expression differences among
214 individuals and/or fibroblast lines.
215 Taken together, the loss of Stx5S results in irregular localization of glycosyltransferases to the Golgi apparatus.
216 An altered Golgi organization and mislocalization of glycosyltransferases can have a profound impact on
217 glycosylation as shown by computational simulations[37]. We investigated the organization of the Golgi complex
218 in Stx5M55V fibroblasts in more detail.
219
220 ***Stx5S mediates retrograde Golgi-ER and intra-Golgi trafficking***
221 Transmission electron microscopy showed dilation of rough ER and Golgi cisternae in the Stx5M55V patient
222 fibroblasts (Fig. 4a-c, gallery Supplementary Fig. 9), similar to previously observed alteration in the ultrastructure
223 of the Golgi in several COG defects[38–40]. Notwithstanding these large alterations in Golgi morphology, the
224 polarized arrangement of Golgi apparatus cisternae was still present in Stx5M55V, as observed by
225 immunofluorescence labeling of *cis*- and *trans*-Golgi markers (Supplementary Fig. 10). These results indicate that
226 although Stx5L is sufficient to maintain normal Golgi apparatus cisterna polarization, Stx5S is required for
227 physiological ER and Golgi ultrastructure and proper trafficking of glycosylation enzymes.
228 To address the role of the Stx5 isoforms in more detail, we studied the distribution of Stx5 isoforms in the Golgi
229 network. Because Stx5L contains an RKR ER-retrieval motif in its N-terminal extension, it locates more at the ER
230 compared to Stx5S[13,18,20,21]. In line with this, we observed a more dominant localization of Stx5L at the ER and
231 less at various Golgi compartments in Stx5M55V fibroblasts compared to total Stx5 localization in healthy control
232 fibroblasts (Supplementary Fig. 11a, b, d, e, Supplementary Fig. 12a, b, d, e).
233 A notable difference was the far more diffuse staining in Stx5M55V patients of the COPI coat protein βCOP
234 (Supplementary Fig. 11a, c) and of TGN46 (Supplementary Fig. 11d, f). In contrast, we observed a small increase
235 in GM130 fluorescence in Stx5M55V patients (Supplementary Fig. 12f). Since Western blot showed that total
236 cellular levels of βCOP and GM130 were not consistently altered in Stx5M55V patients (Supplementary Fig. 11g),
237 the more diffuse staining of βCOP is suggestive of reduced association with COPI-coated vesicles, while the
238 higher staining intensity of GM130 suggests more association with the *cis*-Golgi. In contrast, total TGN46 protein
239 levels were somewhat reduced in patient fibroblasts (Supplementary Fig. 11h). These findings suggest that loss
240 of Stx5S results in reduced COPI trafficking between GM130-marked *cis*- and TGN46-marked *trans*-Golgi
241 compartments.

242 Using an antibody specific to Stx5L (antibody specificity validated in Supplementary Fig. 13), we next investigated
243 whether the loss of Stx5S affects the intracellular distribution of Stx5L. An altered cellular localization of Stx5L
244 might imply a compensatory mechanism. Indeed, in Stx5M55V, Stx5L localizes more to the *cis*-Golgi as measured
245 by increased colocalization with GM130 (Fig. 4d, e). A slight increase in ER localization as measured by PDI
246 colocalization was also observed (Fig. 4f, g). Taken together, the loss of Stx5S causes Stx5L to relocalize more
247 towards the *cis*-Golgi.
248 As COPI is involved in retrograde Golgi-ER transport[41], we investigated whether trafficking at this interface is
249 compromised in Stx5M55V fibroblasts by using the fungal metabolite Brefeldin A (BFA), which inhibits COPI
250 vesicle formation[42]. If loss of Stx5S results in reduced retrograde Golgi-ER transport, we expect reduced
251 relocalization of Golgi-resident proteins to ER upon BFA treatment. Indeed, redistribution of GALNT2 from the
252 Golgi to the ER was incomplete in patient fibroblasts (Fig. 5a-c), supporting a role for Stx5S in retrograde COPI
253 trafficking. In addition, washout of BFA caused a more rapid localization of GALNT2 to the Golgi apparatus in
254 Stx5M55V, likely due to its incomplete redistribution to the ER (Fig. 5a, b, d, Supplementary Fig. 14a-c). We
255 investigated the role of Stx5L in Golgi trafficking further using temperature-synchronizable vesicular stomatitis
256 virus G protein (VSVG) fused to GFP[43] in patient fibroblasts. At 40ºC, VSVG does not fold correctly and the VSVG-
257 GFP protein remains trapped in the ER. A temperature shift to 32ºC enables the correct refolding of VSVG
258 resulting in the synchronized release of VSVG-GFP from the ER, transit through the Golgi network, and finally
259 delivery at the plasma membrane where it becomes accessible to antibody labeling. VSVG-EGFP appears at a
260 Golgi-like compartment in both control and Stx5M55V fibroblasts at 30 mins after temperature shift from 40°C
261 to 32°C (Supplementary Fig. 14d), but after 60 mins plasma membrane localization of VSVG is strongly reduced
262 in Stx5M55V fibroblasts (Fig. 5e-g). Taken together, these findings show that Stx5L is sufficient for anterograde
263 trafficking until the Golgi, but the loss of Stx5S significantly impairs intra- and/or post-Golgi trafficking, likely by
264 the decrease of Stx5S-mediated intra-Golgi trafficking.
265 To further delineate the role of Stx5L in retrograde Golgi-ER trafficking, we performed a BFA experiment in the
266 Stx5L-lacking HeLa cells. In these cells, BFA resulted in faster relocalization of GALNT2 to the ER compared to
267 parental HeLa (Supplementary Fig. 15a, b), indicating that Stx5S suffices for retrograde COPI trafficking and the
268 expression of Stx5L counteracts this process. Further investigation of anterograde ER-Golgi trafficking in Stx5ΔL
269 cells with H-89 washout (Supplementary Fig. 15c, d), the retention using selective hooks (RUSH) system for
270 synchronized ER-Golgi transport[44] (Supplementary Fig. 15e, f, Supplementary Movies 1, 2) and temperature-

271 synchronizable VSVG[43] (Supplementary Fig. 15g, h, Supplementary Movies 3, 4) revealed no phenotype relating
272 to the loss of Stx5L. Thus, these data suggest Stx5L has no necessary function in ER-Golgi trafficking as Stx5S can
273 compensate, while Stx5L can only partly compensate for the loss of Stx5S in retrograde Golgi-ER and intra-Golgi
274 transport.
275
276 ***Faster Golgi exit of Stx5L due to ER-retrieval motif***
277 Our results in patient fibroblasts indicate differential trafficking roles of the two Stx5 isoforms in ER-Golgi
278 trafficking. To gain more insight in this process, we fused each Stx5 isoform to streptavidin-binding protein (SBP)
279 and mCitrine (Stx5L-SBP-mCitrine and Stx5S-SBP-mCitrine; Stx5L-SBP-mCitrine carries the M55V mutation to
280 suppress expression of Stx5S). Moreover, we generated a mutant form of Stx5L where the RKR ER-retrieval motif
281 was converted to 3x alanine (AAA) (Stx5LΔER-SBP-mCitrine)[18], to delineate the role of this motif in ER-Golgi
282 transport. The co-expression of these constructs with ER-localized streptavidin enabled the synchronized release
283 of the Stx5 fusion proteins from the ER using biotin, which is the so-called RUSH system[44] (Fig. 6a). Co-expressing
284 each Stx5 isoform with the Golgi marker Giantin fused to mScarlet[45] in HeLa cells, allowed to visualize the
285 trafficking of Stx5-SBP-mCitrine to the Golgi following the addition of biotin (Fig. 6a, b, Supplementary Movies
286 5-7). All three constructs were expressed at similar levels, as judged from the fluorescent intensities, and all Stx5
287 forms reached the Golgi with the same rate and achieved maximal Golgi localization after about 20 minutes (Fig.
288 6c). However, the subsequent decrease in Golgi localization, attributed to recycling to the ER or degradation of
289 the fusion proteins, was faster for Stx5L-SBP-mCitrine than for Stx5S or Stx5LΔER (Fig. 6c, d). Thus, the RKR ER
290 retrieval motif of Stx5L is necessary and sufficient for the attenuated presence of Stx5L at the Golgi, supporting
291 that the main role of Stx5S is COPI trafficking specifically at the Golgi.
292
293 ***The two isoforms of Stx5 differently engage in SNARE complexes***
294 Since interactions of Stx5 with Bet1 and Bet1L mediate anterograde ER-Golgi transport and retrograde intra-
295 Golgi transport, respectively[2–5], we hypothesized that Stx5S would interact more strongly with Bet1L, whereas
296 Stx5L would interact more strongly with Bet1. We set out to test this hypothesis by performing co-
297 immunoprecipitation with our RUSH Stx5 constructs. However, we were unable to consistently resolve
298 differences in binding to endogenous cognate Qc-SNAREs between the two Stx5 isoforms, either with or without
299 30 mins biotin (Supplementary Fig. 16). A likely explanation is that interactions might occur *in vitro* during the

300 immunoprecipitation. Therefore, we developed an approach to visualize SNARE complexes based on a
301 combination of the RUSH system[44] and our previously developed Förster resonance energy transfer-
302 fluorescence lifetime imaging microscopy (FRET-FLIM) approach for visualization of SNARE complexes[46] (Fig. 7a).
303 This FRET-FLIM approach employed Stx5 isoforms C-terminally fused with a donor fluorophore (mCitrine) and
304 Bet1L C-terminally fused with an acceptor fluorophore (mCherry). The formation of a post-fusion SNARE
305 complex results in the close proximity of the donor and an acceptor fluorophore resulting in FRET which can be
306 measured from a decreased donor fluorescence lifetime (τ). Contrary to ratiometric FRET, FRET-FLIM is not
307 dependent on local concentration differences or excitation intensities of the donor and acceptor fluorophores,
308 as τ is an intrinsic property of the fluorophore itself. By combining the FRET-FLIM approach with the RUSH
309 system, we were able to control the spatial localization of Stx5 isoforms and measure interactions specifically at
310 the ER (no biotin) or the Golgi apparatus (20 min after biotin addition). 30 minutes prior to imaging, cells were
311 incubated with cycloheximide in culture medium to make sure background interaction from any ER-localized
312 newly-synthesized acceptor construct was mitigated.
313 For the mCitrine donor-only Stx5 constructs, we measured similar lifetimes for both isoforms (Fig. 7c,
314 Supplementary Fig. 17a, Stx5L: 3.02 ns ± 0.004, Stx5S: 2.99 ns ± 0.007) prior to biotin addition, while these
315 lifetimes slightly decreased following biotin addition (Fig. 7d, Supplementary Fig. 17a, Stx5L: 2.90 ns ± 0.006,
316 Stx5S: 2.86 ns ±0.011). We attribute this reduced lifetime to the fact that mCitrine is somewhat pH-sensitive[47]
317 and the pH of the Golgi apparatus is lower than in the ER lumen[48]. We then co-expressed the Stx5 isoforms with
318 mCherry-tagged Bet1L (Bet1L-mCherry) (Fig. 7a,b). At the ER, thus before the release of Stx5 with biotin, we
319 observed reduced lifetimes for both Stx5S and Stx5L with Bet1L-mCherry, compared to the donor-only controls
320 (Fig. 7b, c, Stx5L: 2.82 ns ± 0.01, Stx5S: 2.79 ± 0.01), whereas the lifetimes of Stx5S and Stx5L did not significantly
321 differ from each other. After the release in the presence of biotin, this difference between Stx5L and Stx5S
322 became significant and lifetimes were 2.63 ns (± 0.01) for Stx5L while Stx5S dropped to 2.52 ns (± 0.03) (Fig. 7b,
323 d). To validate that the observed effect is indeed caused by functional SNARE complex formation, we repeated
324 this experiment with VAMP8 instead of Bet1L as the acceptor R-SNARE. VAMP8 has no role in ER-Golgi
325 membrane fusion but rather associates with the late endosomal/lysosomal compartment[33,46,49–53]. We only
326 observed minor decreases in fluorescence lifetimes for both Stx5L and Stx5S (Supplementary Fig. 17b, c, prior
327 to biotin Stx5L: 2.92 ns ± 0.01, Stx5S: 2.86 ± 0.02, upon biotin addition Supplementary Fig. 17b, d, Stx5L: 2.82 ns

328 ± 0.01, Stx5S: 2.76 ± 0.02). These FLIM results demonstrate that Stx5S interacts more strongly with Bet1L at the
329 Golgi than Stx5L. Thus, Stx5S is the dominant Qa-SNARE for intra-Golgi trafficking.
330
331 **Discussion**
332 Since the advent of the genomic age, close to 6,000 monogenic disorders have been discovered[54]. While nearly
333 all of these disorders result in a truncated, unstable and/or nonfunctional protein, e.g., due to a genetic variant
334 in the catalytic site or protein misfolding, isoform-specific mutations are rare. Here we present the first known
335 mutation in an alternate site of ribosomal translation leading to human disease, namely the mutation of the
336 second starting methionine of Stx5. This mutation leads to the complete and specific loss of Stx5S. Although
337 *STX5* is an essential gene for embryonic development in mice[16,17], here we show that in humans the loss of Stx5S
338 still allowed a completed pregnancy. Nevertheless, patients have a very severe clinical pathology characterized
339 by infantile mortality due to liver disease, skeletal abnormalities and protein glycosylation defects. While the
340 exact mechanism for alternative translation is unclear, this might be an actively regulated process. It could also
341 be simply regulated by the affinity of the ribosome for the nucleotide sequence upstream of the starting codon.
342 Supporting the latter option, analysis of translation initiation sites with NetStart[55] revealed that the starting
343 codon of Stx5S is located in a more optimal nucleotide context than the starting codon for Stx5L (Supplementary
344 Fig. 18). This could lead to more leaky ribosomal scanning[56,57], resulting in the more or less equimolar ratio of
345 expression of Stx5L and Stx5S that we observed in fibroblasts and PBMCs of healthy individuals. On the other
346 hand, Western blot revealed different ratios of the two Stx5 isoforms in different organs in rats[18], suggesting (i)
347 that different cell types express different levels of Stx5S and Stx5L and this is probably related to their exocytic
348 function, and (ii) that the initiation of starting translation might be regulated and not merely dependent on the
349 binding affinities of the ribosome.
350 Cofractionation and microscopy studies have revealed that the localization of Stx5L and Stx5S overlap to a large
351 extent, but that they are generally distributed as a gradient between ER, ERGIC, and Golgi apparatus[20]. This
352 observation has previously led to the suggestion that Stx5L might play a role in early Golgi trafficking, while Stx5S
353 functions in late Golgi trafficking[5,7,9–13,15,24,31]. Our data now shows that this is not the case and that both Stx5
354 isoforms can mediate both early and late anterograde and retrograde Golgi trafficking with sufficient fidelity to
355 keep the layered Golgi morphology intact. However, the role of Stx5S is more important for retrograde Golgi-ER
356 and intra-Golgi trafficking, and its absence leads to an altered ER and Golgi morphology, distribution of

357 glycosylation enzymes and trafficking proteins. The cumulative effect of slight mislocalization of all
358 glycosyltransferases might well explain the observed hypoglycosylation in the Stx5M55V patients. Indeed,
359 recent modeling showed that the slight mislocalization of glycosyltransferases can result in large differences in
360 glycosylation patterns, because glycosylation is the result of the sequential addition and removal of different
361 sugar moieties at the various Golgi compartments[37].
362 The dominant role of Stx5S in retrograde Golgi-ER and intra-Golgi trafficking is corroborated by the observation
363 that cellular levels of Bet1L, with known roles in intra-Golgi trafficking, are lower in Stx5M55V patient cells.
364 Interestingly, genetic variants in conserved oligomeric Golgi (COG) tethering complex components, which are
365 also implicated in CDGs, also resulted in lower levels of Bet1L as well and this was attributed to a mislocalization
366 of Bet1L to the ER where it was degraded[58]. Possibly, a similar mechanism might explain the reduction in Bet1L
367 levels in Stx5M55V patients. Although the Stx5-Bet1L interaction has been reported in several studies[14,41], our
368 study now shows this interaction *in situ* using FLIM. This interaction is localization dependent and occurs mostly
369 when Stx5 is localized at the Golgi. Moreover, we observed stronger interaction of Bet1L with Stx5S compared
370 to Stx5L at the Golgi, which is likely the result of the differential localization of both isoforms.
371 An important function of the Golgi apparatus is protein glycosylation[59]. Collectively, somatic mutations affecting
372 glycosylation are classified as CDGs and currently over 100 monogenic diseases affecting glycosylation have been
373 identified[60,61]. A significant number of these include defects in Golgi trafficking, such as the components of the
374 conserved oligomeric Golgi tethering complex (COG)[38,62–69], mutations in genes coding for the vacuolar H^+-
375 ATPase and its assembly factors[70–73], and novel genes involved in Golgi ion homeostasis[74–76]. Furthermore,
376 defects are known in components associated with COPI-coated vesicles[77] that result in deficient protein
377 glycosylation in patient cells, but are not linked to abnormal glycosylation of proteins in plasma and thus escape
378 routine CDG screening. Our study is the first example of an ER-Golgi SNARE being implicated in CDG, thus
379 highlighting the potential of glycosylation screening in patients to uncover novel cell biological mechanisms.
380 While the cellular effects of the loss of Stx5S in Stx5M55V mutant fibroblasts are subtle, there can be
381 pronounced consequences in secretory cells, such as exocrine and endocrine cells, which are sensitive to minor
382 disruptions of the secretory pathway[59,77–79]. Not only can the defects in intra-Golgi trafficking explain the
383 hypoglycosylation in Stx5M55V patients, but also of other pathologies. For instance, Stx5 can participate in the
384 trafficking and processing of the very low-density lipoprotein receptor (VLDL-R) and this role is heavily

385 dependent on the expression of Stx5[80], thus providing an explanation for the observed cholesterol homeostasis
386 defect with elevated cholesterol in all Stx5M55V patients.
387 In summary, we have demonstrated that a mutation in an alternative translation start site in Stx5 has a severe
388 impact on intracellular membrane trafficking, leading to the discovery of a novel CDG. While there are many
389 previous descriptions of alternative start site variations leading to disease[81], this is the first known mutation in
390 an alternative starting codon leading to human disease by the loss of an isoform.
391

392 **Acknowledgments**

393 We thank the family for participating in this study. We thank the following people for constructs: Hesso Farhan
394 and Franck Perez (Str-KDEL_ManII-SBP-EGFP; Addgene plasmid #65252), Jennifer Lippincott-Schwartz (pEGFP-
395 VSVG; Addgene plasmid #11912), Feng Zhang (pSpCas9n(BB)-2A-Puro (PX462) V2.0; Addgene plasmid #62987)
396 and Dorus Gadella (pmScarlet-i_Giantin_C1, Addgene plasmid #85050). We also thank the Microscopic Imaging
397 Center of the Radboud Institute for Molecular Life Sciences for use of their microscopy facilities. N.H.R. is funded
398 by a Long-Term Fellowship from the European Molecular Biology Organization (EMBO-LTF, ALTF 232-2016) and
399 a Veni grant from the Netherlands Organization for Scientific Research (016.VENI.171.097). G.v.d.B. is funded by
400 a Young Investigator Grant from the Human Frontier Science Program (HFSP; RGY0080/2018) and a Vidi grant
401 from the Netherlands Organisation for Scientific Research (NWO-ALW VIDI 864.14.001). G.v.d.B has also
402 received funding from the European Research Council (ERC) under the European Union's Horizon 2020 research
403 and innovation program (grant agreement No. 862137). D.J.L. is funded by a Vidi grant (ZONMW VIDI
404 917.13.359), a ZONMW Medium Investment Grant (40-00506-98-9001) from the Netherlands Organisation for
405 Scientific Research, and Erare grants EUROCDG2 and Euroglycanomics. K.Õ, M-A.V., S.P., and K.M. were
406 supported by the Estonian Research Council grants GARLA8175, PUT355, PUTJD827 and PRG471.
407

408 **Author Contributions**

409 P.T.A.L., M.t.B., D.J.L., and G.v.d.B. designed the experiments and wrote the paper. E.C.F.G. contributed to the
410 Stx5 kinetics, co-immunoprecipitation, and FLIM experiments. A.A., M.-A.V., M.B., F.Z., K.H., K.R., K.M., and K.Õ.
411 contributed to the clinical data, exome sequencing and glycomics. O.F. and S.P. performed homozygosity
412 mapping and prioritization of exome variants. N.H.R. and R.d.B. performed TEM. R.A. contributed to the Stx5ΔL

experiments. P.T.A.L. and M.t.B. performed all other experiments. All authors contributed to writing the manuscript.

Declaration of Interests

The authors declare that they have no competing financial interests.

Methods

Ethics

The study was approved by Research Ethics Committee of the University of Tartu (approval dates 19.12.2011, 20.02.2012 and 17.03.2014, and approval numbers 210/M-17, 212/M-31 and 235/M-13, 17.03.2014, respectively) and were strictly in accordance with the Declaration of Helsinki. Informed consent for carrying out research was obtained from the family of investigated individuals. Buffy coats and whole blood were obtained as anonymous coded specimens from the Dutch blood bank (Sanquin) and were handled according to known practice and legal guidelines. The research with human blood samples at the Department of Tumor Immunology complies with all institutional and national ethics regulations and has been approved by the ethics committee of Sanquin.

Glycosylation studies

Screening for CDG was carried out as described before[71]. Plasma N-glycan profiling was performed by MALDI-TOF mass spectrometry of permethylated glycans[82], using 10 µL of plasma. High resolution mass spectrometry of intact transferrin was performed on a 6540 nanochip QTOF (Agilent), according to published protocols[83].

Microarray analysis

DNA was extracted either from peripheral blood according to the standard salting out protocol (IV:9 and IV-:10) or from amnionic fluid cell culture (IV:8). Screening for chromosomal abnormalities was performed using HumanCytoSNP-12 BeadChips (Illumina Inc., San Diego, CA, USA). 200 ng of total DNA per sample was processed according to the protocol supplied by the manufacturer. Genotypes were called by GenomeStudio v2011.1 software and the data were analyzed using GenomeStudio Genome Viewer tool (Illumina Inc.). The minimum threshold for LCSH (long contiguous stretches of homozygosity) regions was set at 5 Mb.

442

443 *Exome sequencing*

444 Genomic DNA was extracted from fibroblasts from patient IV:9 according to the manufacturer's protocol using
445 a Qiagen Mini Kit (Qiagen) and was checked for DNA degradation on agarose gels. Next generation sequencing
446 (NGS) and analysis were performed as described[72]. In brief, exome enrichment was performed using the
447 SureSelect Human All Exon 50 Mb Kit (Agilent), covering ~21,000 genes. The exome library was sequenced on a
448 SOLiD 5500xl sequencer (Life Technologies). Color space reads were iteratively mapped to the hg19 reference
449 genome with the SOLiD LifeScope software version 2.1. Called variants and indels were annotated using an in-
450 house annotation pipeline[84,85] and common variants were filtered out based on a frequency of >0.5% in dbSNP
451 and a frequency of >0.3 % in our in-house database of >5,000 exomes. Quality criteria were applied to filter out
452 variants with less than 5 variant reads and less than 20% variation. Furthermore, synonymous variants, deep
453 intronic, intergenic and UTR variants were excluded. The identified variant was confirmed by Sanger sequencing
454 in all affected individuals (IV:8, IV:9, and IV:10) and their mother (III:2). Paternal DNA (III:1) was not available.

455

456 *Cell culture*

457 HeLa cells (authenticated by ATCC through their human STR profiling cell authentication service), including
458 Stx5ΔL cell lines, were maintained in high glucose DMEM with Glutamax (Gibco 31966021). Human primary
459 dermal fibroblasts were obtained from patients or healthy donors and maintained in Medium 199 with EBSS and
460 L-glutamine (Lonza BE12-119F). All media were supplemented with 10% fetal calf serum (FCS, Greiner Bio-one,
461 Kremsmünster, Austria) and antibiotic-antimycotic solution (Gibco 15240-062). All cells were regularly tested
462 for mycoplasma contamination. Human peripheral blood mononuclear cells (PBMCs) were obtained from buffy
463 coats as previously described[86].

464

465 *Plasmids and transfection*

466 Str-KDEL_ManII-SBP-EGFP was a gift from Franck Perez (Addgene plasmid #65252). VAMP8-mCherry was
467 constructed earlier[46] and previously deposited to Addgene (Addgene plasmid #92424). Str-KDEL_Stx5L-SBP-
468 mCitrine and Str-KDEL_Stx5S-SBP-mCitrine were constructed by replacing the ManII-SBP-EGFP cassette in Str-
469 KDEL_ManII-SBP-EGFP using the AscI and XbaI restriction sites. Stx5 coding sequences were codon-optimized
470 for *Homo sapiens* using JCat and ordered from Genscript, the Stx5L coding sequence carries the M55V mutation

471 to suppress production of Stx5S. Stx5LΔER coding sequence was generated with Q5-polymerase site-directed
472 mutagenesis, using the Stx5L cDNA as a template with the following primer: 5'- CTTCG AATTC AATGA TTCCG
473 GCCGC CGCCT ACGGC AGCAA GAACA CC. Sequences were verified with Sanger sequencing. HeLa cells were
474 transfected with plasmid vectors using Fugene HD (Promega E2311), using the recommended protocol of the
475 manufacturer. Only cells expressing low to moderate levels of the transfected plasmids, based on fluorescence
476 intensity and manual localization scoring, were chosen for subsequent microscopic analyses.
477
478 *CRISPR/Cas9*
479 Stable knock out of Stx5L in fibroblasts and HeLa cells was obtained using the CRISPR-CAS9 method. For this,
480 pairs of gRNA sequences were designed upstream of the *STX5* initiation codon (crispr.mit.edu, pair 1: ATAAC
481 CTCGG ACTGT TGTGG AGG and ATGAT CCCGC GGAAA CGCTA CGG; pair 2: TAACC TCGGA CTGTT GTGGA GGG
482 and TGATC CCGCG GAAAC GCTAC GGG). The gRNA sequences were cloned in pSpCas9n(BB)-2A-Puro (PX462)
483 V2.0 (gift from Feng Zhang, Addgene no. 62987)[87] and transfected into fibroblasts or HeLa cells by
484 electroporation (Neon Transfection System, Thermofisher, MA). After initial selection with puromycin, the
485 medium was changed for conditioned medium (collected from parental fibroblasts or wildtype HeLa cells at 70%
486 confluency) supplemented 1:1 with fresh medium. Single clones were obtained and screened for knockout of
487 Stx5L by SDS-PAGE and Western blotting.
488
489 *Immunofluorescence*
490 Cells were plated on cleaned 12 mm glass coverslips (Electron Microscopy Services, 72230-01) and the following
491 day fixed with 4% paraformaldehyde for 15 minutes at room temperature. Following quenching with 50 mM
492 NH_4Cl in PBS, cells were permeabilized and blocked in 2% normal donkey serum (Rockland, 017-000-121) and
493 0.1% saponin (permeabilization buffer) for 30 mins at RT. Primary and secondary antibodies (list of antibodies
494 and dilutions in Supplementary Table 6) were diluted in permeabilization buffer and incubated for 1 hour at
495 room temperature. Finally, cells were washed with 0.1% Triton X-100 in PBS to remove background staining and
496 mounted with mounting medium containing 0.01% Trolox (6-hydroxy-2,5,7,8-tetramethylchroman-2-carboxylic
497 acid) and 68% glycerol in 200 mM sodium phosphate buffer at pH 7.5 with 0.1 µg/ml DAPI. Coverslips were
498 sealed with nail polish. Cells were imaged on a Leica SP8 SMD confocal laser scanning microscope, equipped

499 with an HC PL APO CS2 63x/1.20 WATER objective. Colocalization analysis was performed using the *pearsonr*
500 function from the Python package SciPy[88]. Briefly, individual cells were saved to separate .tiff files with ImageJ
501 without any modifications, and then processed in a fully automated and unbiased fashion using the *pearsonr*
502 function.
503
504 *Lectin stainings*
505 Cells were plated on cleaned 12 mm glass coverslips for microscopy or 6-wells plates for flow cytometry and
506 after 72 hours culturing fixed with 4% paraformaldehyde. Cells were blocked with Carbo-Free Blocking solution
507 (Vector Laboratories, SP-5040) and incubated with 4 µg/mL biotinylated SNA-I (Vector Laboratories, B-1305) or
508 PNA (Vector Laboratories, B-1075) diluted in Carbo-Free Blocking solution. Cells were then incubated with
509 Streptavidin-Alexa Fluor 647 (ThermoScientific, S32357) before coverslips were mounted as described above.
510 Cells were imaged on a Leica SP8 SMD confocal laser scanning microscope, equipped with an HC PL APO CS2
511 63x/1.20 WATER objective. For flow cytometry, cells were resuspended in FACS buffer (phosphate buffered
512 saline + 0.5% FBS + 0.01% NaN_3). Flow cytometry samples were run on a FACSLyric flow cytometer (BD
513 Biosciences) and analyzed with FlowJo X (FlowJo, LLC).
514
515 *Brefeldin A assay*
516 Fibroblasts were plated in black clear-bottom 96-wells plates (Greiner, 655090) and cultured until 80%
517 confluent. Cells were either treated with 10 µg/mL Brefeldin A in DMSO (Cayman Chemicals, 11861) or DMSO
518 alone for 6 minutes in a humified incubator. Washout was performed by washing five times with Leibovitz's L-
519 15 (Gibco 21083027) with 10% FBS, then incubating in Leibovitz's L-15 with 10% FBS at 37°C for the indicated
520 times. After incubation, plates were transferred immediately to ice and cells were fixed with 4%
521 paraformaldehyde, after which the above immunofluorescence protocol was performed. Microscopy images
522 were acquired using a a Leica SP8 SMD confocal laser scanning microscope, equipped with an HC PL APO CS2
523 63x/1.20 WATER objective. HeLa cells were plated on 12 mm coverslips and incubated in the same way with
524 Brefeldin A, but fixed with 100% methanol at -20°C for 15 mins. Imaging of these samples was performed using
525 a Leica DMI6000B epifluorescence microscope equipped with an HC PL APO 63x1.40 OIL objective. Cells were
526 analyzed using Fiji (http://fiji.sc/) by first removing noise outliers (bright outliers, radius 2.0 pixels, threshold 50),

527 then manually selecting cells and measuring the maximum fluorescence intensity in these ROIs. Data were
528 normalized to the mean of the DMSO control of each group.
529
530 *H-89 assay*
531 HeLa cells were plated on 12 mm coverslips and incubated the following day for 30 mins with 100 µM H-89
532 (Cayman Chemicals, 10010556) in DMSO or DMSO alone (vehicle) and H-89 was washed out with fresh medium
533 for 5 mins. Cells were fixed with 4% paraformaldehyde for 15 mins at RT and permeabilized with 100% methanol
534 at -20°C for 15 mins prior to immunostaining with ERGIC53 mouse monoclonal antibody (G1/93 or OTI1A8)
535 before epifluorescence imaging as described for the BFA assay. Cells were analyzed using Fiji and the number of
536 ERGIC53-positive spots was quantified with the Spot Counter plugin. Data were normalized to the mean
537 fluorescence of the DMSO control of each group. Data was analyzed with a Mann-Whitney U non-parametric
538 test.
539
540 *Transmission electron microscopy*
541 Fibroblasts were grown in 12-wells plates and fixed with 2% glutaraldehyde (Sigma-Aldrich, G5882) in PB (0.1 M
542 phosphate buffer, pH 7.4) for 60 mins at room temperature. Subsequently, cells were washed four times with
543 PB and post-fixed with 1% osmium tetroxide and 1% potassium ferrocyanide in PB for 60 mins at room
544 temperature. Then, cells were again washed four times with PB and four times with water. Cells were incubated
545 overnight in 0.5% uranyl acetate and dehydrated with graded steps of ethanol (30%, 50%, 70%, 96%, 100%) and
546 embedded in Epon resin. 70 nm sections were stained with 2% uranyl acetate solution and lead citrate solution.
547 Stained sections were then examined using a CM12 transmission electron microscope (Phillips).
548
549 *Live-cell epifluorescence microscopy*
550 Cells were seeded in four-compartment dishes (Greiner 627870) and transfected as described above (3:1 weight
551 ratio reporter construct:Golgi label). Before imaging, the culture medium was exchanged for Leibovitz's L-15
552 (Gibco 21083027). Samples were imaged using a DMI6000B (Leica Microsystems) with a heated stage (Pecon)
553 and objective heater. All samples were imaged using an HC PL APO 63x/1.40–0.60 OIL objective. VSVG-ts045-
554 EGFP experiments were performed at 32°C after overnight incubation at 40°C, while all other epifluorescence
555 experiments were performed at 37°C. For RUSH experiments, an equal amount of Leibovitz's L-15 supplemented

556 with biotin was added to the well immediately before imaging, to reach a final concentration of 40 µM biotin.
557 Live cell imaging was started immediately with 15 sec or 30 sec frame rates. Analysis was performed with Fiji,
558 after registration of the image stacks, the increase in fluorescence was measured in the Golgi area by using the
559 thresholded mScarlet-Giantin signal as an image mask.
560
561 *FRET-FLIM*
562 All imaging took place in Leibovitz's L-15 supplemented with 10 µg/mL cycloheximide (Sigma-Aldrich, C4859)
563 and cells were pulsed with biotin as described above. Imaging was performed on a Leica SP8 SMD system at
564 37°C, equipped with an HC PL APO CS2 63x/1.20 WATER objective. Fluorophores were excited with a pulsed
565 white light laser, operating at 80 MHz. mCitrine was excited at 514 nm, two separate HyD detectors were used
566 to collect photons, set at 521-565 nm and 613-668 nm respectively. Photons were collected for one minute and
567 lifetime histograms of the donor fluorophore were fitted with monoexponential decay functions convoluted
568 with the microscope instrument response function in Leica LAS X.
569
570 *Immunoprecipitation*
571 HeLa cells were lysed 48 hours post-transfection with IP lysis buffer (20 mM Tris-HCl pH 7.6, 137 mM NaCl, 1%
572 IGEPAL, 2 mM EDTA and complete protease inhibitors (Roche 5892791001)). Protein levels were equilibrated
573 and lysates were immunoprecipitated with 1 µg anti-GFP-antibody (Rockland 600-401-215) and protein A beads
574 (ThermoFisher, 20333) for 1 hour at 4°C with constant agitation. After three washes with IP lysis buffer, samples
575 were boiled in 5x SDS sample buffer with β-mercaptoethanol and resolved with SDS-PAGE and subsequent
576 immunoblotting.
577
578 *SDS-PAGE and immunoblotting*
579 Cells were plated in 12-wells plates in culture medium and lysed the following day with SDS lysis buffer (1% SDS,
580 10 mM Tris-HCl pH 6.8). Lysates were diluted to equal protein content (30 µg per lane) with SDS lysis buffer,
581 separated with SDS-PAGE on 4–20% Mini-PROTEAN TGX Precast Protein Gels (Biorad, 4561094) and
582 subsequently transferred onto 0.45 µm PVDF membranes. Small molecular weight proteins (Bet1 and Bet1L)
583 were separated on 16% Schaegger gels[89].
584

585 *Quantification and statistical analysis*

586 All mean values represent the average of all cells analyzed. All comparisons between two groups were first
587 checked for similar mean and median values and acceptable (< 3x) difference in variance, before statistical
588 analysis with an unpaired two-sided Student's t-test. Relative intensity data was first transformed using the
589 binary logarithm before analysis with an unpaired two-sided Student's t-test. H-89 data was analyzed with a
590 Mann-Whitney U non-parametric test. Stx5 kinetics data were analyzed with a one-way ANOVA, followed by a
591 post-hoc Tukey's honestly significant difference test. Stx5 FLIM data were analyzed with a two-way ANOVA, with
592 the isoform and timepoint as independent variables, followed by a post-hoc Tukey's honestly significant
593 difference test. $p < 0.05$ was considered significant. *$p < 0.05$, **$p < 0.01$, ***$p < 0.001$, ****$p \leq 0.0001$. All
594 statistical analyses were performed using R statistical software. All numerical data were visualized using R
595 package *ggplot2*[90], with violins representing the overall distribution of the data and means ± 95% CI overlaid.

596

597 *Data and code availability*

598 Microarray data, exome sequencing data and ImageJ macros for quantification of the RUSH experiments are
599 available upon request. Primary microscopy data was deposited to Zenodo.

600 **Figures**

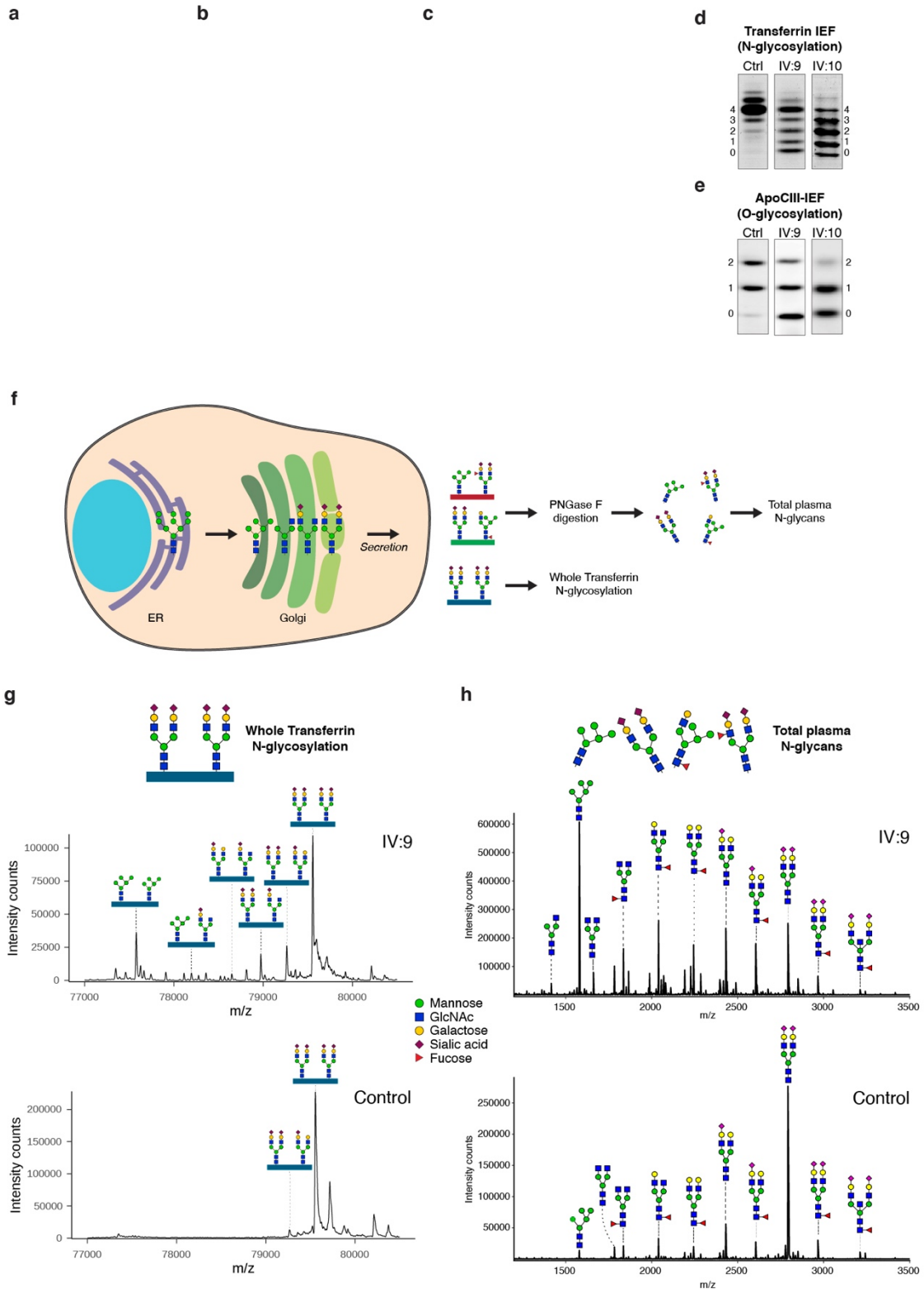

601 **Figure 1. A novel, lethal, genetic variant suggests a defect in protein glycosylation related to Golgi trafficking.**

602 (a-c) Clinical images of Stx5M55V patients IV:8 (a), IV:9 (b), IV:10 (c).

603 (d) Glycosylation screening by isoelectric focusing (IEF) of serum transferrin. The accompanying numbers
604 represent the total number of sialic acids in the different proteoforms. Both patients show a reduction in the
605 number of sialic acids. Quantification of bands is shown in Supplementary Table 2.
606 (e) Glycosylation screening by IEF of serum Apolipoprotein C3 (ApoCIII). ApoCIII has one mucin-type O-linked
607 glycan with one or two sialic acids in controls. Both patients show a reduction in the number of sialic acids.
608 Quantification of bands is shown in Supplementary Table 2.
609 (f) Schematic overview of N-glycosylation intermediates in the Golgi. For mass spectrometry analysis of glycan
610 structures, glycosylated transferrin was enriched from all secreted glycoproteins in human serum and subjected
611 to intact protein mass spectrometry. In parallel, a different serum sample was treated with PNGase F to cleave
612 and analyze N-glycans from all plasma proteins.
613 (g) Nanochip-C8 QTOF mass spectra of enriched intact serum Transferrin of Stx5M55V patient IV:9 (top
614 spectrum) and healthy control (lower spectrum). Key transferrin glycoforms are shown, indicating a strong
615 increase of high-mannose glycans and glycans lacking sialic acid and galactose. Annotation of all peaks of
616 patients IV:9 and IV:10 is shown in Supplementary Table 3.
617 (h) MALDI-TOF mass spectra of total plasma N-glycans of Stx5M55V patient IV:9 (top spectrum) and healthy
618 control (lower spectrum). Structural analysis shows a strong increase of high-mannose glycans and glycans
619 lacking sialic acid and galactose. Annotation of all peaks of patients IV:9 and IV:10 is shown in Supplementary
620 Table 4.
621

622

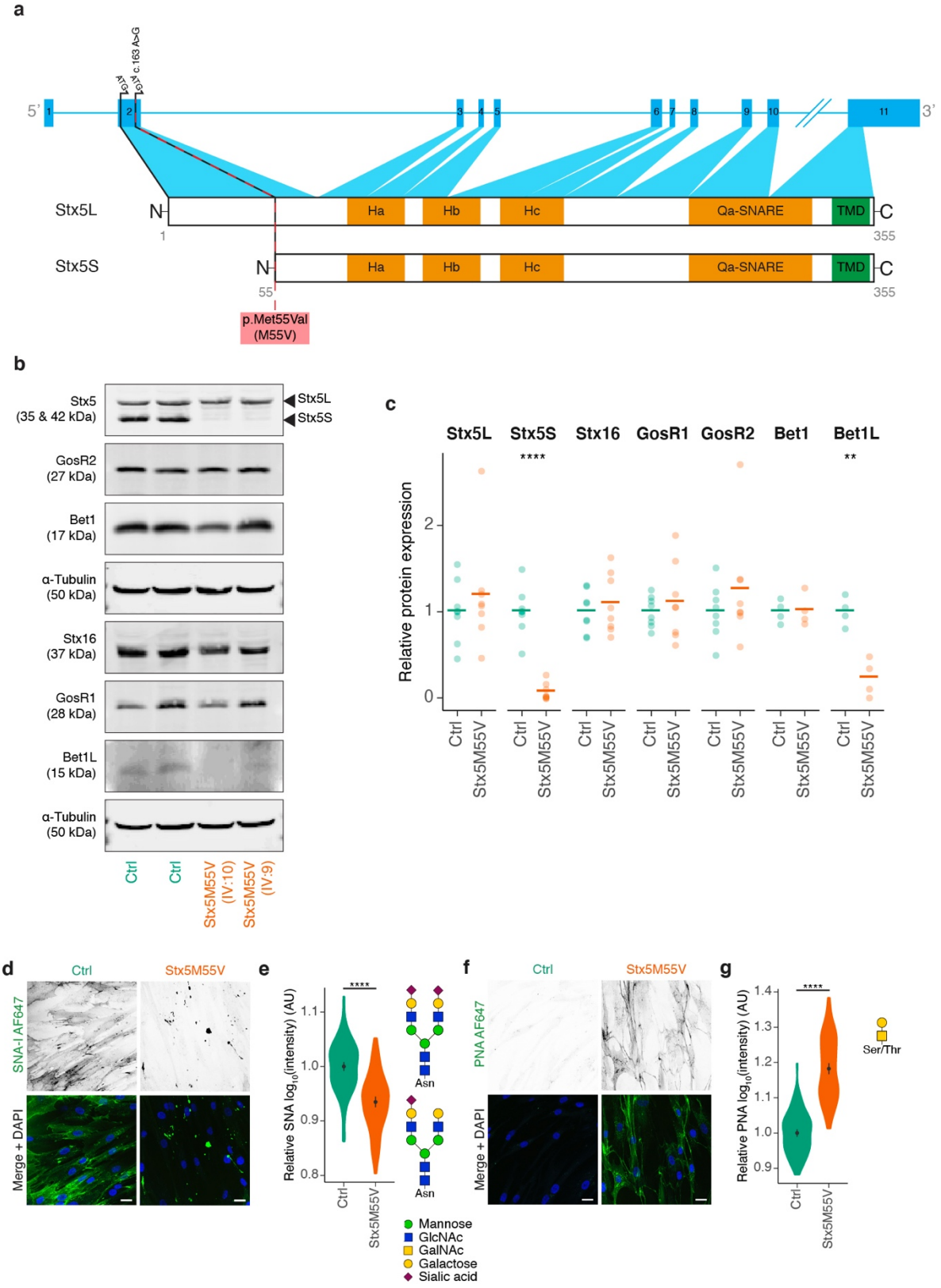
a
c.163 A>G
5'
3'
Stx5L
N
C
Ha
Hb
Hc
Qa-SNARE
TMD
1
355
Stx5S
55
p.Met55Val
(M55V)
b
Stx5
(35 & 42 kDa)
Stx5L
Stx5S
GosR2
(27 kDa)
Bet1
(17 kDa)
α-Tubulin
(50 kDa)
Stx16
(37 kDa)
GosR1
(28 kDa)
Bet1L
(15 kDa)
α-Tubulin
(50 kDa)
Ctrl
Ctrl
Stx5M55V
(IV:10)
Stx5M55V
(IV:9)
c
Stx5L
Stx5S
Stx16
GosR1
GosR2
Bet1
Bet1L
****
**
Relative protein expression
Ctrl
Stx5M55V
d
Ctrl
Stx5M55V
SNA-I AF647
Merge + DAPI
e
****
Relative SNA log10(intensity) (AU)
Asn
Asn
Mannose
GlcNAc
GalNAc
Galactose
Sialic acid
f
Ctrl
Stx5M55V
PNA AF647
Merge + DAPI
g
****
Relative PNA log10(intensity) (AU)
Ser/Thr

623

624 **Figure 2. Primary dermal fibroblasts are an accurate model of the glycosylation defect observed in Stx5M55V**
625 **patients.**

626 (a) Schematic representation of the intron-exon structure of *STX5* and the encoded proteoforms resulting from
627 the two starting codons in exon 2. The Stx5M55V genetic variant is indicated by a dashed red line. Orange regions
628 have a secondary helical structure. TMD, transmembrane domain. Ha, Hb, Hc: regulatory Habc-domain.

629 (b) Representative immunoblot for SNARE proteins of cell lysates of primary human dermal fibroblasts from two
630 unique individual healthy donors (green, Ctrl) or Stx5M55V patients (orange, Stx5M55V). α-Tubulin, loading
631 control.

632 (c) Quantification of (b). Protein levels were first normalized to the loading control, then to the average
633 expression of both control lines. Each point represents one cell line from 2 independent experiments.

634 (d) Fibroblasts of healthy donors (green, Ctrl) or Stx5M55V patients (orange, Stx5M55V) were probed with SNA-
635 I lectin (green in merge). Representative confocal micrographs. Scalebars, 25 µm. DAPI in blue.

636 (e) Quantification of (d). All data were log_{10}-transformed and then normalized to the healthy donor. N = 124
637 (Ctrl) and 111 (Stx5M55V) cells from 2 unique individuals tested twice.

638 (f-g) Same as panels (d-e), but now for PNA lectin. N = 117 (Ctrl) and 122 (Stx5M55V) cells from 2 unique
639 individuals tested twice**.**

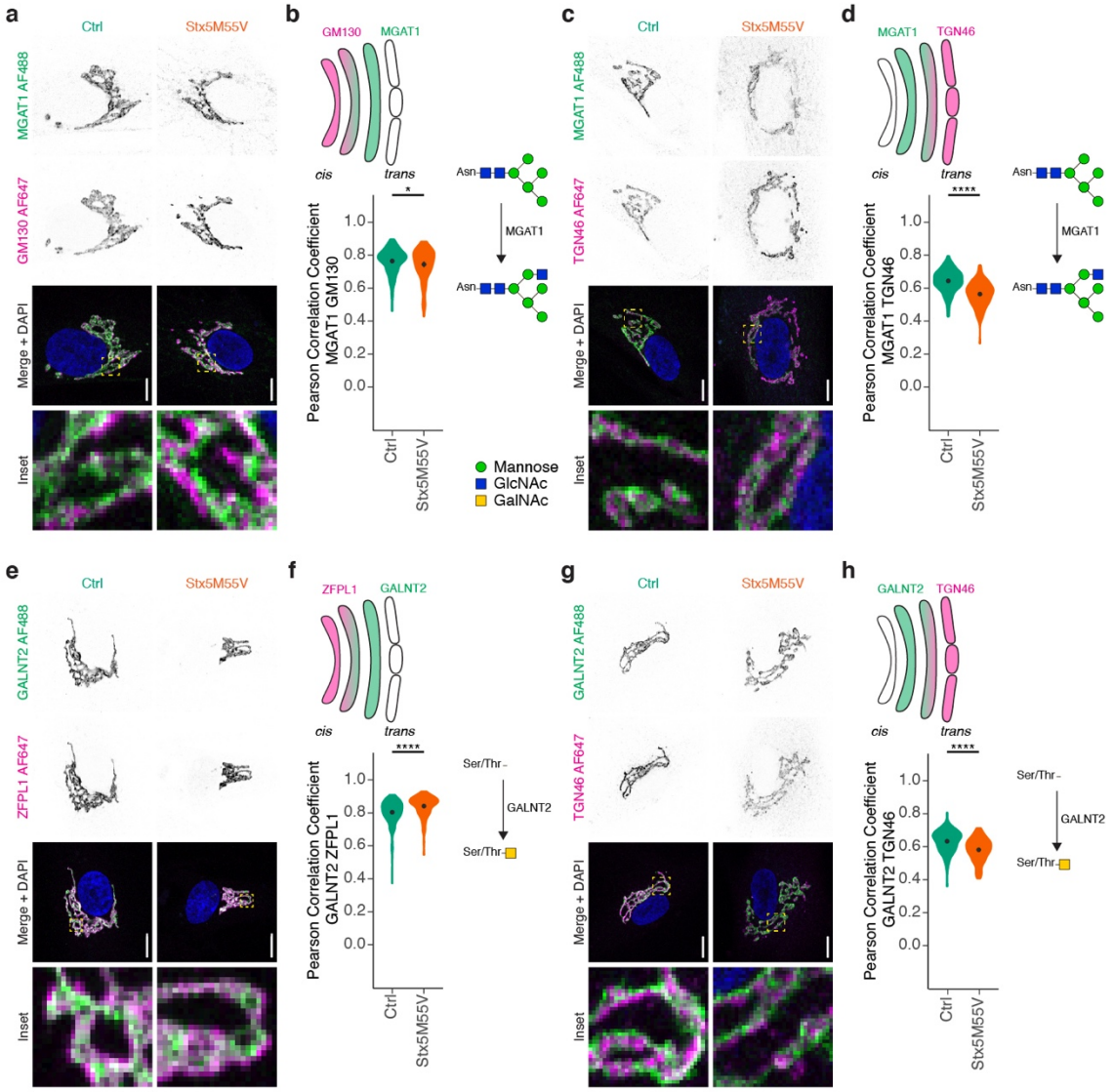

Figure 3. Glycosylation enzymes mislocalize in Stx5M55V patient fibroblasts.

(a) Immunofluorescence microscopy of MGAT1 (green in merge) and GM130 (magenta) in primary dermal fibroblasts of healthy donors (green, Ctrl) or Stx5M55V patients (orange, Stx5M55V). Representative confocal micrographs. Scalebars, 10 µm. DAPI in blue. N = 157 (Ctrl) and 126 (Stx5M55V) cells from 2 unique individuals tested twice.

(b) Pearson's correlations coefficients between MGAT1 and GM130 of panel (a). N = 157 (Ctrl) and 126 (Stx5M55V) from 2 unique individuals tested twice.

(c-d) Same as panels (a-b), but now for MGAT1 (green) and TGN46 (magenta). N = 157 (Ctrl) and 162 (Stx5M55V) cells from 2 unique individuals tested twice.

650 (e-f) Same as panels (a-b), but now for GALNT2 (green) and ZFPL1 (magenta). N = 240 (Ctrl) and 146 (Stx5M55V)

651 cells from 2 unique individuals tested twice.

652 (g-h) Same as panels (a-b), but now for GALNT2 (green) and TGN46 (magenta). N = 172 (Ctrl) and 152 (Stx5M55V)

653 cells from 2 unique individuals tested twice.

654

655
656

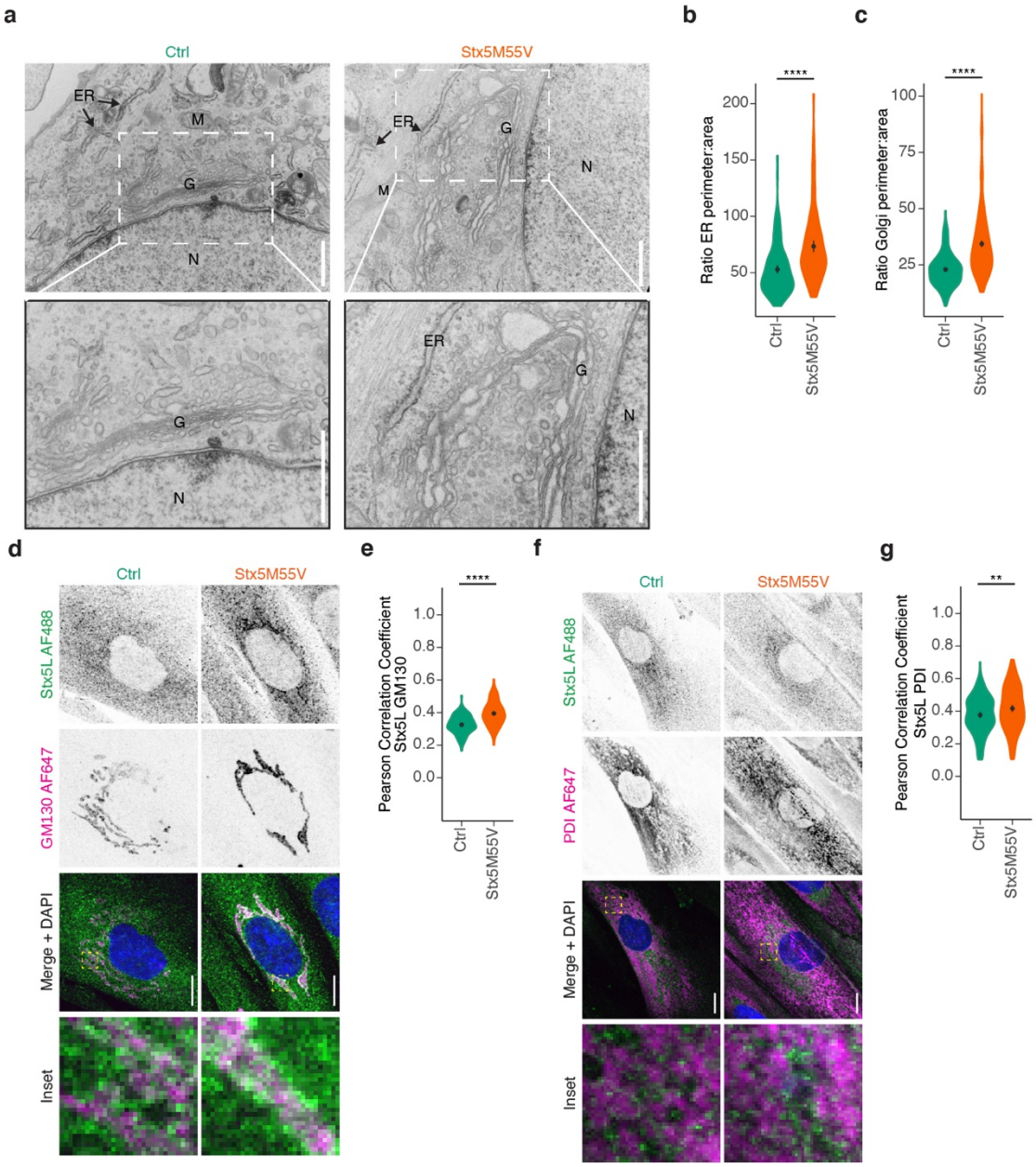

Figure 4. Loss of Stx5S alters ER and Golgi morphology.

(a) Representative transmission electron micrographs from healthy donor fibroblasts (left) or Stx5M55V patient fibroblasts (right). Scalebars, 1 µm. N, nucleus; G, Golgi apparatus; ER, endoplasmic reticulum; M, mitochondrion. More electron micrographs in Supplementary Fig. 9.

(b) ER perimeter and area quantification of panel (a), the ratios of the perimeters over the areas are plotted. N = 144 (both Ctrl and Stx5M55V) ER sections.

(c) Same as panel (b), but now for Golgi. N = 400 (both Ctrl and Stx5M55V) Golgi sections.

664 (d) Immunofluorescence microscopy of Stx5L (green in merge) and GM130 (magenta) in primary dermal
665 fibroblasts of healthy donors (green, Ctrl) or Stx5M55V patients (orange, Stx5M55V). Representative
666 confocal micrographs. Scalebars, 10 µm. DAPI in blue.
667 (e) Pearson's correlations coefficients between Stx5L and GM130 of panel (d). N = 102 (Ctrl) and 135
668 (Stx5M55V) cells from 2 unique individuals tested twice.

669 (f-g) Same as panels (d-e), but now for Stx5L (green) and TGN46 (magenta). N = 147 (Ctrl) and 156
670 (Stx5M55V) from 2 unique individuals tested twice.

671

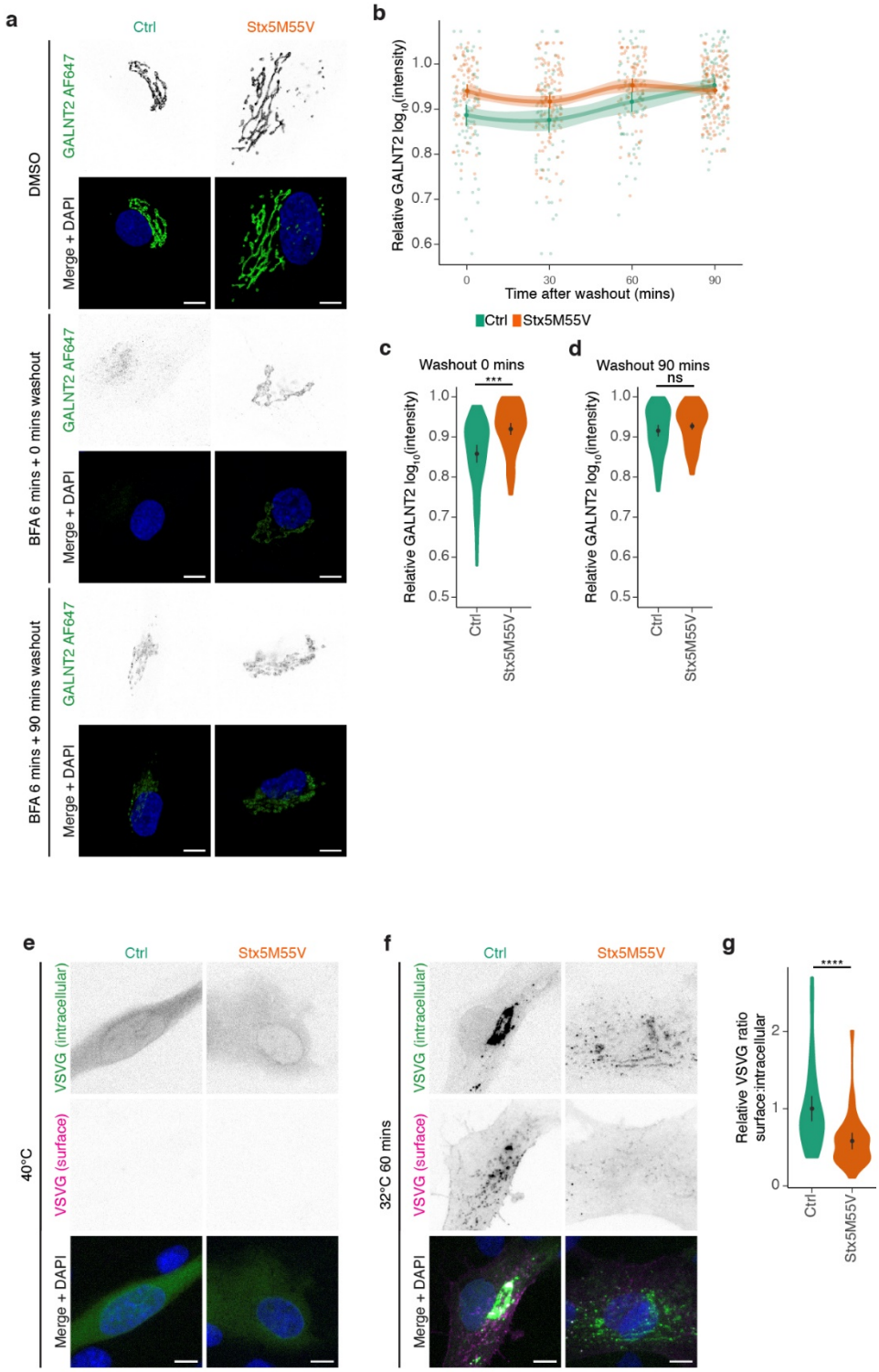

Figure 5. Loss of Stx5S compromises ER-Golgi trafficking.

(a) Immunofluorescence microscopy of GALNT2 (green in merge) in primary human dermal fibroblasts of healthy donors (green, Ctrl) or Stx5M55V patients (orange, Stx5M55V) in the absence or presence of

676 Brefeldin A (BFA) for 6 min and washout for the indicated times. Representative confocal micrographs
677 are shown. Scalebars, 10 µm. DAPI in blue.
678 (b) Timecourse of relative maximum fluorescence intensities of GALNT2 from panel (a). All data were
679 normalized to the DMSO condition (vehicle).
680 (c) Quantification of the 0 min washout timepoint from panels (a) and (b). N = 76 (Ctrl) and 85 (Stx5M55V)
681 cells from 2 unique individuals tested twice.
682 (d) Same as (c), but now for the 90 min timepoint. N = 97 (Ctrl) and 152 (Stx5M55V) cells from 2 unique
683 individuals tested twice.
684 (e) Immunofluorescence microscopy of VSVG-EGFP in primary human dermal fibroblasts of healthy donors
685 (green, Ctrl) or Stx5M55V patients (orange, Stx5M55V) cultured overnight at 40°C. Representative
686 confocal micrographs are shown. Scalebars, 10 µm. DAPI in blue.
687 (f) Same as (e), but now after 60 mins at 32°C.
688 (g) Quantification of the ratio of surface to intracellular of VSVG after 60 mins at 32°C. N = 45 (Ctrl) and 39
689 (Stx5M55V) cells from 2 unique individuals tested twice.
690

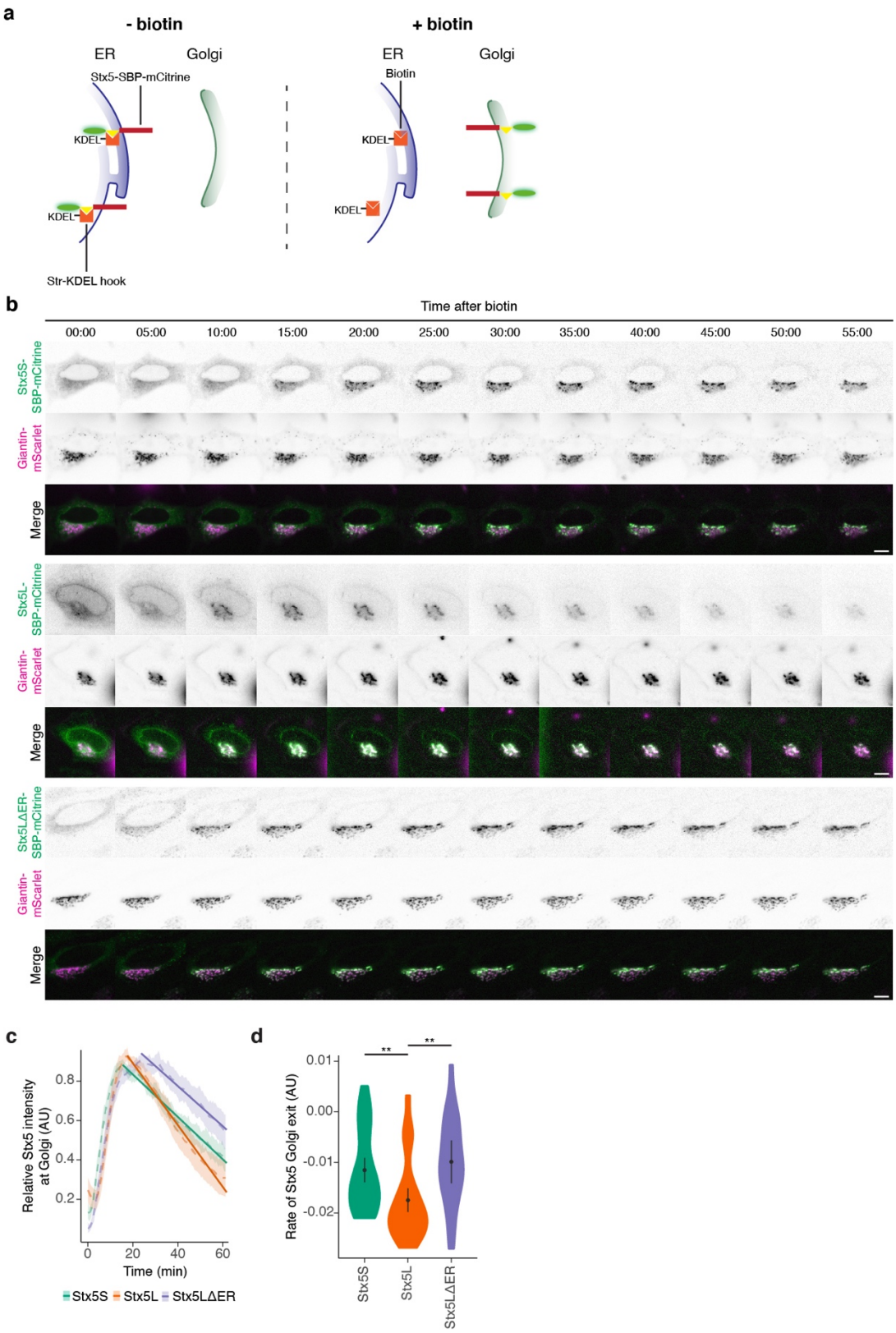

691 **Figure 6. Faster Golgi exit of Stx5L than Stx5S.**

692 (a) Schematic overview of the design of Stx5 trafficking experiment, based on the RUSH system. In absence of

693 biotin (left panel), the reporter cargo (Stx5-SBP-mCitrine) is trapped at the ER by the lumenal Str-KDEL hook.

694 When biotin is added (right panel), biotin outcompetes the interaction with streptavidin, allowing Stx5-SBP-
695 mCitrine to traffic freely to its destination compartment. SBP, streptavidin binding protein; Str, streptavidin.
696 (b) Snapshots of live-cell imaging of Stx5-SBP-mCitrine (green in merge). Magenta: Golgi marker Giantin-
697 mScarlet. Scale bars, 10 µm. See also supplementary movies 5 – 7.

698 (c) Quantification of mCitrine fluorescence at the Golgi of Stx5S-SBP-mCitrine (green), Stx5L-SBP-mCitrine
699 (orange) and Stx5LΔER-SBP-mCitrine (blue) over time from panel (b). N = 44 (Stx5S), 47 (Stx5L) and 19 (Stx5ΔER)
700 cells from 4 independent experiments.

701 (d) Quantification of the slopes from panel (c) of the post-Golgi section (~20 mins onwards).
702

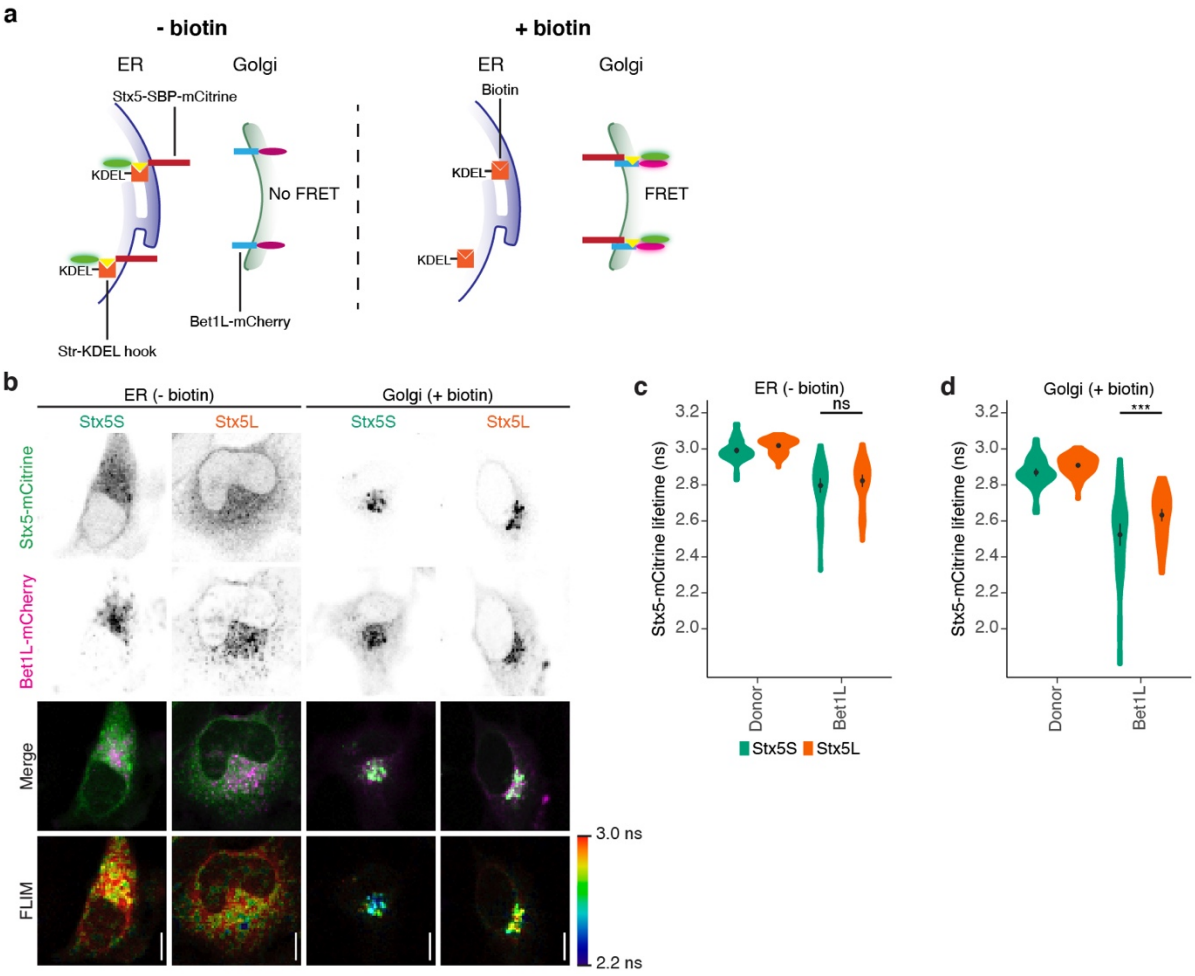

Figure 7. Stx5S is the dominant Qa-SNARE for intra-Golgi trafficking.

(a) Schematic overview of experimental design for complex formation of Stx5 isoforms with Bet1L, based on the RUSH system and SNARE complex measurement by FRET-FLIM. In absence of biotin (left panel), the reporter cargo (Stx5-SBP-mCitrine) is trapped at the ER by the lumenal Str-KDEL hook, and no FRET with Golgi-localized Bet1L-mCherry occurs. When biotin is added (right panel), biotin outcompetes the interaction with streptavidin, allowing Stx5-SBP-mCitrine to traffic freely to its destination compartment, and SNARE complex formation with Golgi-localized Bet1L-mCherry results in FRET. SBP, streptavidin binding protein; Str, streptavidin; FRET, Förster resonant energy transfer. FLIM, fluorescence lifetime imaging microscopy.

(b) Representative confocal micrographs of HeLa cells co-expressing Stx5-mCitrine (green in merge) and Bet1L-mCherry (magenta) without (ER) or with (Golgi) biotin. Scalebars, 10 µm.

(c-d) Stx5-mCitrine lifetimes at the ER (c) and Golgi (d) from panel (b). N = 52 (Stx5S Donor ER), 74 (Stx5L Donor ER), 47 (Stx5S Bet1L ER), 51 (Stx5L Bet1L ER), 50 (Stx5S Donor Golgi), 71 (Stx5L Donor Golgi), 58 (Stx5S Bet1L Golgi) and 58 (Stx5L Bet1L Golgi) cells from 3 independent experiments.

717 **References**

718 1. Jahn, R. & Scheller, R. H. SNAREs — engines for membrane fusion. *Nature Reviews*
719 *Molecular Cell Biology* **7**, 631–631 (2006).
720 2. Banfield, D. K., Lewis, M. J. & Pelham, H. R. B. A SNARE-like protein required for traffic
721 through the Golgi complex. *Nature* **375**, 806–809 (1995).
722 3. Parlati, F. *et al.* Topological restriction of SNARE-dependent membrane fusion. *Nature*
723 **407**, 194–198 (2000).
724 4. Parlati, F. *et al.* Distinct SNARE complexes mediating membrane fusion in Golgi transport
725 based on combinatorial specificity. *Proceedings of the National Academy of Sciences of*
726 *the United States of America* **99**, 5424–9 (2002).
727 5. Xu, Y., Martin, S., James, D. E. & Hong, W. GS15 Forms a SNARE Complex with Syntaxin
728 5, GS28, and Ykt6 and Is Implicated in Traffic in the Early Cisternae of the Golgi
729 Apparatus. *MBoC* **13**, 3493–3507 (2002).
730 6. Bentley, M. *et al.* SNARE status regulates tether recruitment and function in homotypic
731 COPII vesicle fusion. *The Journal of biological chemistry* **281**, 38825–33 (2006).
732 7. Dascher, C., Matteson, J. & Balch, W. E. Syntaxin 5 regulates endoplasmic reticulum to
733 Golgi transport. *The Journal of biological chemistry* **269**, 29363–6 (1994).
734 8. Rowe, T., Dascher, C., Bannykh, S., Plutner, H. & Balch, W. E. Role of vesicle-associated
735 syntaxin 5 in the assembly of pre-Golgi intermediates. *Science (New York, N.Y.)* **279**,
736 696–700 (1998).
737 9. Xu, D., Joglekar, A. P., Williams, A. L. & Hay, J. C. Subunit structure of a mammalian
738 ER/Golgi SNARE complex. *The Journal of biological chemistry* **275**, 39631–9 (2000).
739 10. Hay, J. C. *et al.* Localization, Dynamics, and Protein Interactions Reveal Distinct Roles for
740 ER and Golgi SNAREs. *The Journal of Cell Biology* **141**, 1489–1502 (1998).

741 11. Paek, I. *et al.* ERS-24, a Mammalian v-SNARE Implicated in Vesicle Traffic between the
742 ER and the Golgi. *The Journal of Cell Biology* **137**, 1017–1028 (1997).
743 12. Zhang, T. *et al.* Ykt6 forms a SNARE complex with syntaxin 5, GS28, and Bet1 and
744 participates in a late stage in endoplasmic reticulum-Golgi transport. *The Journal of*
745 *biological chemistry* **276**, 27480–7 (2001).
746 13. Linders, P. T., van der Horst, C., ter Beest, M. & van den Bogaart, G. Stx5-Mediated ER-
747 Golgi Transport in Mammals and Yeast. *Cells* **8**, 780 (2019).
748 14. Malsam, J. & Söllner, T. H. Organization of SNAREs within the Golgi stack. *Cold Spring*
749 *Harbor perspectives in biology* **3**, a005249–a005249 (2011).
750 15. Tai, G. *et al.* Participation of the Syntaxin 5/Ykt6/GS28/GS15 SNARE Complex in
751 Transport from the Early/Recycling Endosome to the Trans-Golgi Network. *MBoC* **15**,
752 4011–4022 (2004).
753 16. Dickinson, M. E. *et al.* High-throughput discovery of novel developmental phenotypes.
754 *Nature* **537**, 508–514 (2016).
755 17. Koscielny, G. *et al.* The International Mouse Phenotyping Consortium Web Portal, a
756 unified point of access for knockout mice and related phenotyping data. *Nucleic Acids*
757 *Res* **42**, D802–D809 (2014).
758 18. Hui, N. *et al.* An isoform of the Golgi t-SNARE, syntaxin 5, with an endoplasmic reticulum
759 retrieval signal. *Molecular biology of the cell* **8**, 1777–87 (1997).
760 19. Gao, G. & Banfield, D. K. Multiple features within the syntaxin Sed5p mediate its Golgi
761 localization. *Traffic* **21**, 274–296 (2020).
762 20. Dominguez, M. *et al.* gp25L/emp24/p24 protein family members of the cis-Golgi
763 network bind both COP I and II coatomer. *The Journal of cell biology* **140**, 751–65 (1998).

764 21. Miyazaki, K. *et al.* Contribution of the long form of syntaxin 5 to the organization of the
765 endoplasmic reticulum. *Journal of Cell Science* **125**, 5658 LP – 5666 (2012).
766 22. Suga, K., Saito, A., Tomiyama, T., Mori, H. & Akagawa, K. The Syntaxin 5 Isoforms Syx5
767 and Syx5L have Distinct Effects on the Processing of β-amyloid Precursor Protein. *The*
768 *Journal of Biochemistry* **146**, 905–915 (2009).
769 23. Avci, D. *et al.* The intramembrane protease SPP impacts morphology of the endoplasmic
770 reticulum by triggering degradation of morphogenic proteins. *J. Biol. Chem.* **294**, 2786–
771 2800 (2019).
772 24. Hay, J. C., Hirling, H. & Scheller, R. H. Mammalian vesicle trafficking proteins of the
773 endoplasmic reticulum and Golgi apparatus. *J. Biol. Chem.* **271**, 5671–5679 (1996).
774 25. Shestakova, A., Suvorova, E., Pavliv, O., Khaidakova, G. & Lupashin, V. Interaction of the
775 conserved oligomeric Golgi complex with t-SNARE Syntaxin5a/Sed5 enhances intra-Golgi
776 SNARE complex stability. *The Journal of Cell Biology* **179**, 1179–1192 (2007).
777 26. Linders, P. T. A., Peters, E., ter Beest, M., Lefeber, D. J. & van den Bogaart, G. Sugary
778 Logistics Gone Wrong: Membrane Trafficking and Congenital Disorders of Glycosylation.
779 *International Journal of Molecular Sciences* **21**, 4654 (2020).
780 27. Fung, C. W. *et al.* COG5-CDG with a Mild Neurohepatic Presentation. *JIMD Rep* **3**, 67–70
781 (2012).
782 28. Paesold-Burda, P. *et al.* Deficiency in COG5 causes a moderate form of congenital
783 disorders of glycosylation. *Hum. Mol. Genet.* **18**, 4350–4356 (2009).
784 29. Palmigiano, A. *et al.* MALDI-MS profiling of serum O-glycosylation and N-glycosylation in
785 COG5-CDG. *Journal of Mass Spectrometry* **52**, 372–377 (2017).
786 30. Rymen, D. *et al.* COG5-CDG: expanding the clinical spectrum. *Orphanet J Rare Dis* **7**, 94
787 (2012).

788 31. Zhang, T. *et al.* The Mammalian Protein (rbet1) Homologous to Yeast Bet1p Is Primarily
789 Associated with the Pre-Golgi Intermediate Compartment and Is Involved in Vesicular
790 Transport from the Endoplasmic Reticulum to the Golgi Apparatus. *The Journal of Cell*
791 *Biology* **139**, 1157–1168 (1997).
792 32. Mallard, F. *et al.* Early/recycling endosomes-to-TGN transport involves two SNARE
793 complexes and a Rab6 isoform. *The Journal of Cell Biology* **156**, 653–664 (2002).
794 33. Dingjan, I. *et al.* Endosomal and Phagosomal SNAREs. *Physiological Reviews* **98**, 1465–
795 1492 (2018).
796 34. Pokrovskaya, I. D. *et al.* Conserved oligomeric Golgi complex specifically regulates the
797 maintenance of Golgi glycosylation machinery. *Glycobiology* **21**, 1554–1569 (2011).
798 35. Chiu, C.-F. *et al.* ZFPL1, a novel ring finger protein required for cis-Golgi integrity and
799 efficient ER-to-Golgi transport. *The EMBO journal* **27**, 934–47 (2008).
800 36. Gleeson, P. A. *et al.* p230 is associated with vesicles budding from the trans-Golgi
801 network. *Journal of Cell Science* **109**, 2811–2821 (1996).
802 37. Jaiman, A. & Thattai, M. Golgi compartments enable controlled biomolecular assembly
803 using promiscuous enzymes. *eLife* **9**, e49573 (2020).
804 38. Reynders, E. *et al.* Golgi function and dysfunction in the first COG4-deficient CDG type II
805 patient. *Hum Mol Genet* **18**, 3244–3256 (2009).
806 39. Climer, L. K., Pokrovskaya, I. D., Blackburn, J. B. & Lupashin, V. V. Membrane
807 detachment is not essential for COG complex function. *MBoC* **29**, 964–974 (2018).
808 40. Oka, T. *et al.* Genetic Analysis of the Subunit Organization and Function of the
809 Conserved Oligomeric Golgi (COG) Complex STUDIES OF COG5- AND COG7-DEFICIENT
810 MAMMALIAN CELLS. *J. Biol. Chem.* **280**, 32736–32745 (2005).

811 41. Glick, B. S. & Nakano, A. Membrane Traffic Within the Golgi Apparatus. *Annual Review*
812 *of Cell and Developmental Biology* **25**, 113–132 (2009).
813 42. Galea, G., Bexiga, M. G., Panarella, A., O'Neill, E. D. & Simpson, J. C. A high-content
814 screening microscopy approach to dissect the role of Rab proteins in Golgi-to-ER
815 retrograde trafficking. *J Cell Sci* **128**, 2339–2349 (2015).
816 43. Lippincott-Schwartz, J., Roberts, T. H. & Hirschberg, K. Secretory Protein Trafficking and
817 Organelle Dynamics in Living Cells. *Annual Review of Cell and Developmental Biology* **16**,
818 557–589 (2000).
819 44. Boncompain, G. *et al.* Synchronization of secretory protein traffic in populations of cells.
820 *Nature Methods* **9**, 493–493 (2012).
821 45. Bindels, D. S. *et al.* mScarlet: a bright monomeric red fluorescent protein for cellular
822 imaging. *Nature Methods* **14**, 53–56 (2017).
823 46. Verboogen, D. R. J., González Mancha, N., ter Beest, M. & van den Bogaart, G.
824 Fluorescence Lifetime Imaging Microscopy reveals rerouting of SNARE trafficking driving
825 dendritic cell activation. *eLife* **6**, (2017).
826 47. Griesbeck, O., Baird, G. S., Campbell, R. E., Zacharias, D. A. & Tsien, R. Y. Reducing the
827 Environmental Sensitivity of Yellow Fluorescent Protein MECHANISM AND
828 APPLICATIONS. *J. Biol. Chem.* **276**, 29188–29194 (2001).
829 48. Casey, J. R., Grinstein, S. & Orlowski, J. Sensors and regulators of intracellular pH. *Nature*
830 *reviews. Molecular cell biology* **11**, 50–61 (2010).
831 49. Antonin, W., Holroyd, C., Tikkanen, R., Höning, S. & Jahn, R. The R-SNARE
832 Endobrevin/VAMP-8 Mediates Homotypic Fusion of Early Endosomes and Late
833 Endosomes. *MBoC* **11**, 3289–3298 (2000).

834 50. Bajno, L. *et al.* Focal Exocytosis of Vamp3-Containing Vesicles at Sites of Phagosome
835 Formation. *J Cell Biol* **149**, 697–706 (2000).
836 51. Hong, W. SNAREs and traffic. *Biochimica et Biophysica Acta (BBA) - Molecular Cell*
837 *Research* **1744**, 120–144 (2005).
838 52. Manderson, A. P., Kay, J. G., Hammond, L. A., Brown, D. L. & Stow, J. L.
839 Subcompartments of the macrophage recycling endosome direct the differential
840 secretion of IL-6 and TNFα. *J Cell Biol* **178**, 57–69 (2007).
841 53. Murray, R. Z. A Role for the Phagosome in Cytokine Secretion. *Science* **310**, 1492–1495
842 (2005).
843 54. Amberger, J. S., Bocchini, C. A., Schiettecatte, F., Scott, A. F. & Hamosh, A. OMIM.org:
844 Online Mendelian Inheritance in Man (OMIM®), an online catalog of human genes and
845 genetic disorders. *Nucleic Acids Res* **43**, D789–D798 (2015).
846 55. Pedersen, A. G. & Nielsen, H. Neural network prediction of translation initiation sites in
847 eukaryotes: perspectives for EST and genome analysis. *Proc Int Conf Intell Syst Mol Biol*
848 **5**, 226–233 (1997).
849 56. Kochetov, A. V. Alternative translation start sites and hidden coding potential of
850 eukaryotic mRNAs. *BioEssays* **30**, 683–691 (2008).
851 57. Kozak, M. Regulation of translation via mRNA structure in prokaryotes and eukaryotes.
852 *Gene* **361**, 13–37 (2005).
853 58. Oka, T., Ungar, D., Hughson, F. M. & Krieger, M. The COG and COPI Complexes Interact
854 to Control the Abundance of GEARs, a Subset of Golgi Integral Membrane Proteins.
855 *MBoC* **15**, 2423–2435 (2004).
856 59. Ohtsubo, K. & Marth, J. D. Glycosylation in Cellular Mechanisms of Health and Disease.
857 *Cell* **126**, 855–867 (2006).

858 60. Freeze, H. H., Chong, J. X., Bamshad, M. J. & Ng, B. G. Solving Glycosylation Disorders:
859 Fundamental Approaches Reveal Complicated Pathways. *The American Journal of*
860 *Human Genetics* **94**, 161–175 (2014).
861 61. Fisher, P. & Ungar, D. Bridging the Gap between Glycosylation and Vesicle Traffic. *Front.*
862 *Cell Dev. Biol.* **4**, (2016).
863 62. Blackburn, J. B., Kudlyk, T., Pokrovskaya, I. & Lupashin, V. V. More than just sugars:
864 Conserved oligomeric Golgi complex deficiency causes glycosylation-independent
865 cellular defects. *Traffic* **19**, 463–480 (2018).
866 63. Foulquier, F. *et al.* Conserved oligomeric Golgi complex subunit 1 deficiency reveals a
867 previously uncharacterized congenital disorder of glycosylation type II. *PNAS* **103**, 3764–
868 3769 (2006).
869 64. Foulquier, F. *et al.* A new inborn error of glycosylation due to a Cog8 deficiency reveals a
870 critical role for the Cog1–Cog8 interaction in COG complex formation. *Hum Mol Genet*
871 **16**, 717–730 (2007).
872 65. Kranz, C. *et al.* COG8 deficiency causes new congenital disorder of glycosylation type IIh.
873 *Hum Mol Genet* **16**, 731–741 (2007).
874 66. Miller, V. J. & Ungar, D. Re'COG'nition at the Golgi. *Traffic* **13**, 891–897 (2012).
875 67. Morava, E. *et al.* A common mutation in the COG7 gene with a consistent phenotype
876 including microcephaly, adducted thumbs, growth retardation, VSD and episodes of
877 hyperthermia. *Eur J Hum Genet* **15**, 638–645 (2007).
878 68. Ng, B. G. *et al.* Molecular and clinical characterization of a Moroccan Cog7 deficient
879 patient. *Molecular Genetics and Metabolism* **91**, 201–204 (2007).
880 69. Wu, X. *et al.* Mutation of the COG complex subunit gene COG7 causes a lethal
881 congenital disorder. *Nat Med* **10**, 518–523 (2004).

882 70. Hucthagowder, V. *et al.* Loss-of-function mutations in ATP6V0A2 impair vesicular
883 trafficking, tropoelastin secretion and cell survival. *Hum Mol Genet* **18**, 2149–2165
884 (2009).
885 71. Jansen, J. C. *et al.* CCDC115 Deficiency Causes a Disorder of Golgi Homeostasis with
886 Abnormal Protein Glycosylation. *The American Journal of Human Genetics* **98**, 310–321
887 (2016).
888 72. Jansen, J. C. *et al.* TMEM199 Deficiency Is a Disorder of Golgi Homeostasis Characterized
889 by Elevated Aminotransferases, Alkaline Phosphatase, and Cholesterol and Abnormal
890 Glycosylation. *The American Journal of Human Genetics* **98**, 322–330 (2016).
891 73. Jansen, E. J. R. *et al.* ATP6AP1 deficiency causes an immunodeficiency with hepatopathy,
892 cognitive impairment and abnormal protein glycosylation. *Nature Communications* **7**,
893 11600–11600 (2016).
894 74. Foulquier, F. *et al.* TMEM165 Deficiency Causes a Congenital Disorder of Glycosylation.
895 *The American Journal of Human Genetics* **91**, 15–26 (2012).
896 75. Ashikov, A. *et al.* Integrating glycomics and genomics uncovers SLC10A7 as essential
897 factor for bone mineralization by regulating post-Golgi protein transport and
898 glycosylation. *Hum Mol Genet* **27**, 3029–3045 (2018).
899 76. Park, J. H. *et al.* SLC39A8 Deficiency: A Disorder of Manganese Transport and
900 Glycosylation. *The American Journal of Human Genetics* **97**, 894–903 (2015).
901 77. Witkos, T. M. *et al.* GORAB scaffolds COPI at the trans -Golgi for efficient enzyme
902 recycling and correct protein glycosylation. *Nat Commun* **10**, 1–18 (2019).
903 78. Zhong, W. Golgi during Development. *Cold Spring Harb Perspect Biol* **3**, (2011).
904 79. Zhao, H. Membrane Trafficking in Osteoblasts and Osteoclasts: New Avenues for
905 Understanding and Treating Skeletal Diseases. *Traffic* **13**, 1307–1314 (2012).

906 80. Wagner, T., Dieckmann, M., Jaeger, S., Weggen, S. & Pietrzik, C. U. Stx5 is a novel
907 interactor of VLDL-R to affect its intracellular trafficking and processing. *Experimental*
908 *Cell Research* **319**, 1956–1972 (2013).
909 81. Bogaert, A., Fernandez, E. & Gevaert, K. N-Terminal Proteoforms in Human Disease.
910 *Trends in Biochemical Sciences* **45**, 308–320 (2020).
911 82. Morelle, W. & Michalski, J.-C. Analysis of protein glycosylation by mass spectrometry.
912 *Nature Protocols* **2**, 1585–1602 (2007).
913 83. van Scherpenzeel, M., Steenbergen, G., Morava, E., Wevers, R. A. & Lefeber, D. J. High-
914 resolution mass spectrometry glycoprofiling of intact transferrin for diagnosis and
915 subtype identification in the congenital disorders of glycosylation. *Translational*
916 *Research* **166**, 639-649.e1 (2015).
917 84. Vissers, L. E. L. M. *et al.* A de novo paradigm for mental retardation. *Nature Genetics* **42**,
918 1109–1112 (2010).
919 85. Nikopoulos, K. *et al.* Next-Generation Sequencing of a 40 Mb Linkage Interval Reveals
920 TSPAN12 Mutations in Patients with Familial Exudative Vitreoretinopathy. *The American*
921 *Journal of Human Genetics* **86**, 240–247 (2010).
922 86. Jolanda, I., de Vries, M., Adema, G. J., Punt, C. J. A. & Figdor, C. G. Phenotypical and
923 Functional Characterization of Clinical-Grade Dendritic Cells. in *Adoptive*
924 *Immunotherapy: Methods and Protocols* (eds. Ludewig, B. & Hoffmann, M. W.) 113–125
925 (Humana Press, 2005). doi:10.1385/1-59259-862-5:113.
926 87. Ran, F. A. *et al.* Genome engineering using the CRISPR-Cas9 system. *Nature Protocols* **8**,
927 2281–2308 (2013).
928 88. Virtanen, P. *et al.* SciPy 1.0: fundamental algorithms for scientific computing in Python.
929 *Nature Methods* **17**, 261–272 (2020).

89. Schägger, H. Tricine–SDS-PAGE. *Nat Protoc* **1**, 16–22 (2006).

90. Wickham, H. *ggplot2: Elegant Graphics for Data Analysis*. (Springer-Verlag New York, 2016).